

# We are IntechOpen, the world's leading publisher of Open Access books Built by scientists, for scientists

6,900

Open access books available

186,000

International authors and editors

200M

Downloads

Our authors are among the

154

Countries delivered to

TOP 1%

most cited scientists

12.2%

Contributors from top 500 universities



WEB OF SCIENCE™

Selection of our books indexed in the Book Citation Index  
in Web of Science™ Core Collection (BKCI)

Interested in publishing with us?  
Contact [book.department@intechopen.com](mailto:book.department@intechopen.com)

Numbers displayed above are based on latest data collected.  
For more information visit [www.intechopen.com](http://www.intechopen.com)



---

# Photonic Crystals for Optical Sensing: A Review

---

Benedetto Troia, Antonia Paolicelli,  
Francesco De Leonardis and Vittorio M. N. Passaro

Additional information is available at the end of the chapter

<http://dx.doi.org/10.5772/53897>

---

## 1. Introduction

In recent years, photonic sensors have seen a massive development because of the increasing demand of sensing applications in healthcare, defence, security, automotive, aerospace, environment, food quality control, to name a few.

The development and integration of Microfluidic and Photonic technologies, with specific reference to the CMOS-compatible silicon-on-insulator (SOI) technology, allows to enhance sensing performance in terms of sensitivity, limit-of-detection (LOD) and detection multiplexing capability. Photonic sensors have been the subject of intensive research over the last decade especially for detection of a wide variety of biological and chemical agents. In this context, photonic Lab-on-a-chip systems represent the state-of-the-art of photonic sensing since they are expected to exhibit higher sensitivity and selectivity as well as high stability, immunity to electromagnetic interference and product improvements, such as smaller integration sizes and lower costs.

In recent years, rapid advancements in photonic technologies have significantly enhanced sensing performance, particularly in the areas of light-analyte interaction, device miniaturization, multiplexing and fluidic design and integration. This has led to drastic improvements in sensor sensitivity, enhanced limit of detection (LOD), advanced fluidic handling capability, lower sample consumption, faster detection time, and lower overall detection cost per measurement. With future commercialization of photonic biosensors in a Lab-on-a-chip, next generation biosensors are expected to be reliable and portable, able to be fabricated with mass production techniques, to reduce the cost as well as to do multi-parameter analysis, enabling fast and real-time measurements of a large amount of biological or physical parameters within a single, compact sensor chip.

In this context, photonic crystals (PhCs) represent an intriguing solution for achieving high performance in sensing applications. In fact, since a lot of photonic architectures have been widely investigated and employed in photonic sensing (e.g., ring resonator, surface Plasmon resonance (SPR) – based sensors, microdisks, microspheres, to name a few), PhCs exhibit a strong optical confinement of light to a very small volume, enabling the detection of chemical species characterized by nanometer dimensions. In addition, by using advanced chemical surface functionalization techniques and integration with microfluidic systems, very high performance can be achieved in ultra compact sensor chips. For example, the detection of dissolved avidin concentrations as low as 15 nM or 1  $\mu\text{m}/\text{ml}$ , has been experimentally achieved by using functionalized slotted PhC cavities with integrated microfluidics (Scullion et al., 2011). Ultra high performance have been experimentally and theoretically demonstrated, such as a LOD less than 20 pM for anti-biotin, corresponding to less than 4.5 fg of bound material on the sensor surface and fewer than 80 molecules in the modal volume of the integrated microcavity (Zlatanovic et al., 2009).

PhC-based sensors have been also proposed as gas sensors in mid infrared (mid-IR), since many gases (e.g.,  $\text{CO}_2$ ,  $\text{CH}_4$ , CO) exhibit absorption lines in mid-IR wavelength region. Other applications reported in literature concern with the detection of temperature, pressure, stress and humidity measurements, to name a few.

From a technological point of view, photonic sensors based on PhCs, including photonic crystal optical fiber (PCFs) and integrated planar photonic crystals, are suitable for multiplexing and label-free detection. For example, a large-scale chip-integrated PhC sensor microarrays has been recently proposed and demonstrated for biosensing on a SOI-based platform (Zou et al., 2012). Standard and CMOS compatible technological processes (i.e., electron-beam lithography, inductively coupled plasma (ICP) etching, plasma enhanced chemical vapor deposition (PECVD)) are generally employed for PhCs fabrication, making these sensors suitable for mass-scale and low cost production. Finally, PCFs can be easily fabricated by stacking tubes and rods of silica glass into a large structure of the pattern of holes required in the final fiber.

In this chapter, a complete review on planar PhC- and PCF-based sensors, is presented. In particular, it will be focused on the choice of materials and sensing applications.

Optical sensing principles will be described in detail, with particular reference to homogeneous and surface sensing, optical absorption, fluorescence, surface Plasmon resonance (SPR) and photonic detection based on non linear effects (e.g., Four Wave Mixing, Raman effect, surface enhanced Raman scattering). In addition, several advanced waveguide structures and microstructured optical fibers (MOFs) will be analyzed. For example, resonant microcavities based on integrated PhCs, slotted resonant cavities, interferometer configurations (e.g., directional couplers and Mach-Zehnder Interferometer (MZI), Sagnac interferometer), active PhC-based sensing devices, to be named. Sensing applications and performance of PhC-based sensors are reviewed and compared with those exhibited by other conventional photonic architectures in literature. The state of the art of PhC- based sensors is analyzed, highlighting on the actual strategic approach of integrating PhC sensors chips with Optofluidic Microsystems (Choi et al., 2006), and on advanced technologies and measurement setups employed in PCF-based sensing.

## 2. Integrated photonic crystal sensors

Nowadays, integrated PhC-based sensors represent one of the most popular class of photonic sensors, generally employed for physical and chemical/biochemical sensing. In this context, the principal advantages of these intriguing photonic sensor architectures are ultra-high light confinement in very small volumes, high wavelength selectivity, ultra high sensitivity and selectivity in sensing mechanism.

Materials usually employed for sensing PhC planar devices are heteropitaxial layers such as AlGaAs/GaAs, III-nitride compound layers or dielectric layers such as  $\text{Si}_3\text{N}_4$ ,  $\text{TiO}_2$ ,  $\text{SiO}_2$  and the well-known SOI wafers (Biallo et al., 2006). In addition, organic compounds, and polymers have attracted an increasing interest in the last few years. Finally, porous silicon photonic crystals have been recently proposed for organic vapor sensing, too. However, future integrated photonic sensors are expected to be CMOS-compatible, able to be realized with low cost processes, and suitable for mass-scale production.

In this context, the SOI technological platform represents undoubtedly the most suitable platform for fabricating ultra-compact and ultra-high performance PhC-based integrated sensors.

To this purpose, several types of PhC-based sensor architectures are presented in this section, focusing on employed sensing principles (i.e., refractive index (RI)-based sensor, optical absorption, opto-mechanical, nonlinear effects) and application performance.

### 2.1. RI-based PhC sensors

Refractive index based sensors represent the most diffused class of PhC sensors. In fact, a large number of advanced architectures (e.g., integrated microcavities and interferometric configurations) employ the refractive index sensing for detection. RI-based PhC sensors present numerous advantages such as minimal sample preparation without fluorescence labeling, real-time detection, high sensitivity and selectivity. In particular, the sensing principle consists in measuring RI changes of a bulk solution (e.g., deionized water,  $n_{\text{Water}} = 1.33$  or air,  $n_{\text{Air}} = 1$  @  $\lambda = 1.55 \mu\text{m}$ ) due to the presence of chemical analytes or gases generally characterized by higher refractive indices. Applications in gaseous and aqueous environment have been studied to detect concentrations of chemical and biological species. In fact, by using these sensors, it is possible to quantify molecule and protein (e.g., streptavidin, DNA, mRNA) surface or volumetric density. Recently, advanced PhC-based sensors properly designed for single-molecule detection have been demonstrated to be able to detect the number of molecules concentrated into a complex solution (Lin et al., 2012).

In this section, two fundamental sensing principles commonly employed in photonic RI sensing are presented, i.e., surface and homogeneous sensing.

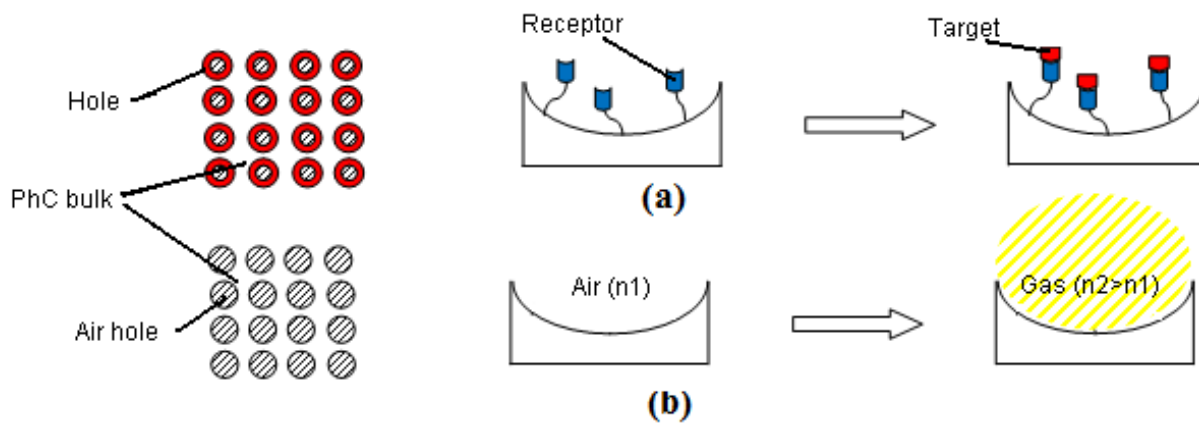


**Figure 1.** a) Surface sensing and (b) homogeneous sensing. Probe molecules (blue) are deposited on hole surfaces and target molecules (red) are captured by receptors forming an adlayer on the sensor surface.

In Fig. 1(a), the surface sensing principle is sketched. In particular, PhC holes are initially functionalized by receptor molecules properly chosen in order to selectively adsorb target analytes in a complex solution. Consequently, when the device is exposed to a chemical sample, target molecules are immobilized by receptors on the sensor hole inner surfaces. The adsorbed layer characterized by a thickness  $t_{ad}$  induces a localized refractive index change around the hole region. Finally, a surface sensitivity  $S_s$  is generally defined as follows:

$$S_s = \frac{\partial n_{eff}}{\partial t_{ad}} \quad (1)$$

where  $n_{eff}$  is the effective index of the optical mode propagating in the sensor device and  $t_{ad}$  has been previously defined.

The remaining sensing mechanism named homogeneous sensing, is schematically sketched in Fig. 1(b). In this case, the effective index of the propagating optical mode changes because of cover RI variations induced by gases or liquid samples properly concentrated in the cover medium, where the photonic sensor is exposed. Consequently, a homogeneous sensitivity  $S_h$  can be defined as follows:

$$S_h = \frac{\partial n_{eff}}{\partial n_c} \quad (2)$$

being  $n_c$  the cover refractive index.

In the following, main architectures of PhC RI-based sensors are presented, focusing on their operating principles and performance.

The first class of sensors to be discussed are those based on photonic crystal resonant microcavities. These devices are fabricated by introducing localized defects (i.e., removing one or

more holes) in the periodic hole distribution. In this way, the perfect periodicity of the photonic crystal is compromised and a defective state in the band gap map is introduced, allowing the excitation of resonance modes.

Two parameters, i.e., the quality factor  $Q$  and the wavelength sensitivity  $S_\lambda$ , have to be considered for appreciating PhC-cavity-based sensor performances. The  $Q$ -factor defines the shape of resonant peaks and consequently the value of the Full Width at Half Maximum (FWHM) and it is expressed as follows:

$$Q = \frac{\omega_0 U(t)}{P(t)}, \text{ or } Q = \frac{f_0}{\Delta f} \quad (3)$$

where  $\omega_0$  is the angular resonant frequency,  $U(t)$  is the energy stored in the cavity mode,  $P(t)$  is the energy dissipated per cycle (i.e., a single roundtrip in the resonant cavity),  $f_0$  is the resonant frequency and  $\Delta f$  is the peak bandwidth.

In particular, PhC-cavity-based sensors can be interrogated into two distinct modes. The first one is the wavelength interrogation mode and the second one is the intensity interrogation mode. In the first method, the optical readout consists in monitoring the wavelength of the optical signal through an optical spectrum analyzer (OSA), while in the latter one, it is possible to monitor the intensity changes of the output signal by using a photodetector (PD). In this context, the wavelength sensitivity  $S_\lambda$  represents a fundamental parameter for quantifying the sensor performance in case of wavelength interrogation scheme.  $S_\lambda$  is defined according to Eq. (4), as the ratio between the shift of resonant wavelength ( $\Delta\lambda$ ) induced by the change of the background refractive index ( $\Delta n$ ). Moreover, it is given in units of nm/RIU (refractive index unit), as:

$$S_\lambda = \frac{\Delta\lambda}{\Delta n} \quad (4)$$

In Fig. 2 a typical example of two-dimensional (2D) PhC microcavity in silicon-on-insulator (SOI) wafer is shown (Liu et al., 2012). As sketched in Fig. 2, air holes are etched only in the upper silicon layer and they can be realized by standard anisotropic etching. The periodic structure is characterized by an hexagonal cell with lattice constant  $a=515 \text{ nm}$ . The radius  $r$  of air holes and the thickness of the silicon layer  $h$  are chosen to be the ratios  $r/a=0.33$  and  $h/a=0.427$ , resulting in  $r=170 \text{ nm}$  and  $h=220 \text{ nm}$ . As it is possible to observe in Fig. 2, the microcavity is obtained by removing seven air holes at the centre of PhC in the  $\Gamma K$  direction. Such microcavity is formally indicated as L7-cavity, because of the number of holes removed in the periodic PhC structure.

Different arrangements of air holes near the cavity centre improve the  $Q$ -factor of the microcavity presented above. In particular, by shifting three rows of air holes in the  $\Gamma M$  direction spaced from the cavity centre of a distance of  $0.02a$ ,  $0.014a$  and  $0.017a$ , it is possible to obtain

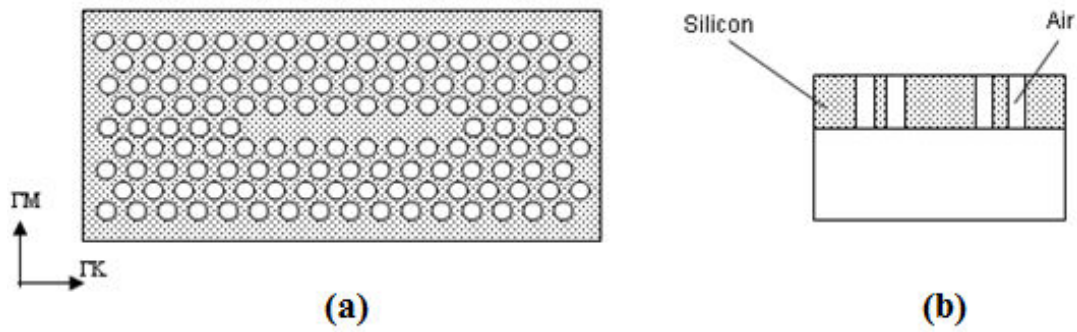


**Figure 2.** PhC microcavity (a) realized by removing seven holes as line defect (L7 cavity) and cross section (b).

an improvement of  $Q$ -factor of a factor  $\sim 1,000$ . In addition, by placing three pairs of mini holes into the cavity region it is possible to further increase the performance of PhC resonant cavity. The image of this new arrangement is sketched in Fig. 3. In particular, the pair named C has a radius  $r_C = 0.78r$  and an outward position shift  $d_C = 0.2a$ . The second pair centre (i.e., B) is not moved, but the radii of these holes are minimized, resulting in  $d_B = 0$  and  $r_B = 0.2r$ . Finally, the innermost pair of holes have a displacement from original position  $d_A = 0.2a$  and a radius slightly larger than previous pair to be  $r_A = 0.28r$ . Under these design conditions, in air-infiltrated case, the cavity achieves a  $Q$ -factor of 2,600, exhibiting a resonant wavelength around 1550 nm.

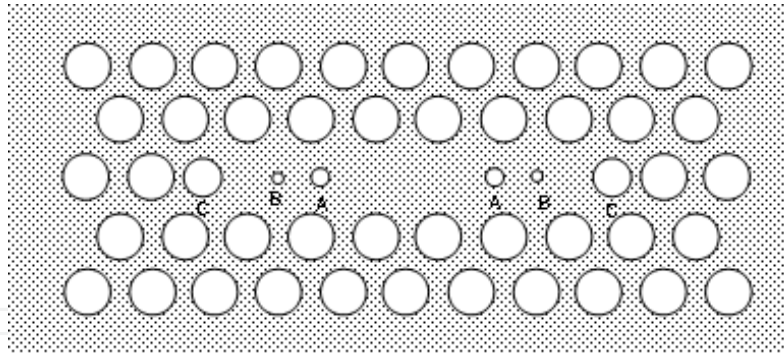


**Figure 3.** Zoom of cavity region of L7 cavity.

Performances of the sensor proposed have been evaluated in case of water or ethanol infiltration, whose refractive indices are estimated to be 1.332 and 1.359 at  $\lambda \approx 1.55 \mu\text{m}$ , respectively. The resonant wavelength shift measured in the first case is 22.28 nm and in the latter is equal to 12.65 nm. Finally, the device described until now exhibits a sensitivity as high as 460 nm/RIU, being larger than sensitivities usually achieved by L3 cavity.

An interesting RI-based sensor employing a PhC resonant microcavity is characterized by a cavity region in an air slot. In this sensor, the technological approach employed for realizing the microcavity does not consist in modifying the lattice constant or the hole radii character-

izing the PhC, but in introducing a straight line defect in which a modified waveguide width acts as resonant cavity (Jágorská et al., 2010).

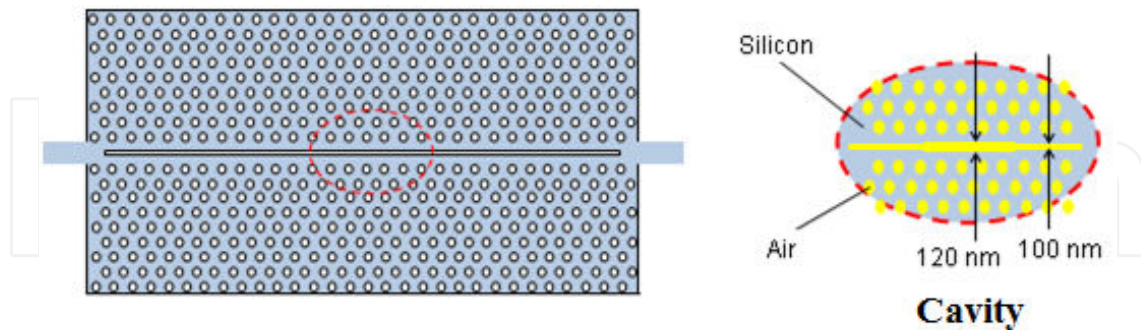


**Figure 4.** Air-slot PhC cavity with zoom of slit in the slot.

As sketched in Fig. 4, the device consists of a 2D PhC characterized by hexagonal cell and lattice constant  $a=510 \text{ nm}$ . The waveguide region is obtained by removing a row of air holes in the middle of the structure. An air – slot is embedded in this line defect region. The width of the air slot is kept constant at 100 nm, except in the middle. A slit is made by increasing the width of air slot from 100 nm to 120 nm, in the centre. This reduction in slot width results in the formation of reflective barriers for traveling mode, thus in a resonant cavity whose length is  $L = 3a$ .

The complete device has been processed on a 220-nm-thick SOI wafer with a 2  $\mu\text{m}$  buried oxide layer. The cavity mode is strongly confined into the cavity region, the effective mode volume is  $V_{\text{eff}}=0.05\mu\text{m}^3$  and the spatial overlapping between cavity mode and air slot is  $\Gamma > 0.73$ .

The sensitivity can be expressed as a function of the spatial mode overlapping  $\Gamma$ , as reported in the following expression:

$$S_{\lambda} = \frac{\Delta\lambda}{\Delta n} = \Gamma \frac{\lambda_0}{n_{\text{eff}}} \quad (5)$$

where  $n_{\text{eff}}^2 = \Gamma n_{\text{gas}}^2 + (1 - \Gamma)n_{\text{Si}}^2$  is the effective index of the cavity mode,  $n_{\text{Si}}=3.46$  is the silicon RI,  $n_{\text{gas}}$  is the gas RI and  $\lambda_0$  is the resonant wavelength. When air characterized by the refractive index  $n_{\text{air}}=1$  is infiltrated in PhC holes, the sensor exhibits the resonance frequency  $\lambda_0=1570 \text{ nm}$ , near to cut-off frequency which occurs at 1590 nm. The quality factor has been estimated to be  $Q=26,000$  and the sensitivity  $S_{\lambda}=570 \text{ nm}/\text{RIU}$ .

Sensor performances have been experimentally quantified by exposing the cavity to different gases. Several gases have been used. In particular, air ( $n = 1.000265$ ) as reference gas, nitrogen ( $\text{N}_2$ ,  $n = 1.000270$ ), helium ( $\text{He}$ ,  $n = 1.000032$ ), carbon dioxide ( $\text{CO}_2$ ,  $n = 1.000406$ ), acetylene ( $\text{C}_2\text{H}_2$ ,  $n = 1.000579$ ) and propane ( $\text{C}_3\text{H}_8$ ,  $n = 1.000999$ ). All refractive indices are given at

atmospheric pressure at the resonant wavelength  $\lambda_0=1570 \text{ nm}$  and room temperature,  $T=20^\circ \text{C}$ .

Experimental results show a blue shift for He gas and a red shift for  $\text{CO}_2$  or  $\text{C}_3\text{H}_8$  gas characterized by higher RIs. In fact, the resonant wavelength shift is demonstrated to be linearly dependent on refractive index changes ( $n_{\text{gas}} - 1$ ) calculated with respect to the reference gas, i.e. air ( $n = 1$ ).

The PhC sensor described above is limited by the fact that resonant wavelength shifts are not only influenced by cover refractive index changes, but also by external parameters such as temperature, pressure, adsorbed humidity or progressive oxidation of sensor surface. In order to minimize this effect, it is necessary to test the sensor with  $\text{O}_2$ -free gases or use an identical sensor architecture acting as a reference one for compensating undesired effects mentioned above.

A PhC sensor based on a ring resonator cavity has been proposed for monitoring the level of seawater salinity between 0% to 40% (Robinson et al., 2012). In particular, a ring resonator is realized by removing a number of silicon rods in the PhC structure characterized by periodic distribution of square cells of silicon rods in air. The sensor architecture is shown in Fig. 5 below.

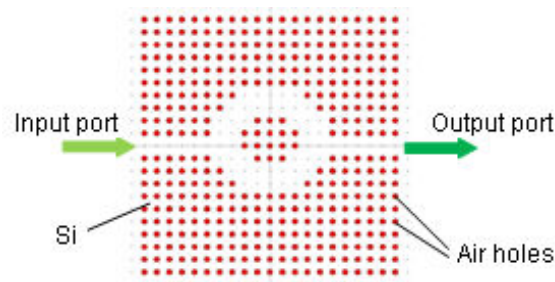


**Figure 5.** Schematic structure of sensor for seawater sensing.

The lattice constant is  $a=540 \text{ nm}$  and radius of rods is  $r=0.185a=100 \text{ nm}$ . The refractive index of silicon rods is  $n = 3.46$  while the background RI is set to be the seawater RI. An input and output waveguides are placed in horizontal direction with respect to the center of the ring cavity.

Different salinity percentages induce background RI changes, resulting in a detectable variation of the sensor transmission spectrum. In particular, it is possible to adopt both an intensity and a wavelength interrogation scheme, resulting in a more accurate and precise optical readout. The output efficiency of the sensor decreases from 99% to 80% by increasing the salt level in water from 0% to 40%. Moreover, in the range of salinity 0÷40%, the water RI increases from 1.33300 to 1.34031, respectively. According to Eq. (4), changes of the background solution RI produce resonant wavelength shifts. In fact, in the range of interest, i.e., 0÷40% the resonant wavelength shifts down from 1590.55 nm to 1590.05 nm. Finally, the  $Q$ -factor changes as a function of the salinity. In fact, by increasing the salt level in water the  $Q$ -factor increases.

A PhC sensor based on an air-bridge cavity has been proposed, exhibiting a good sensitivity (Junhua et al., 2011). The photonic crystal sensor is characterized by a triangular (or equivalently hexagonal) array of air holes with lattice constant  $a=440\text{ nm}$  and radius  $r=0.29a=127.5\text{ nm}$ . The microcavity has been realized by decreasing the radius of the central hole ( $r_d=0.2a=88\text{ nm}$ ). The air-bridge is made by removing a portion of buried silicon dioxide that is sandwiched between two silicon layers, as sketched in Fig. 6. The top silicon layer with thickness  $t=0.591a$  is separated by  $1\text{ }\mu\text{m}$  of  $\text{SiO}_2$  from the second silicon layer on the bottom of the same structure.

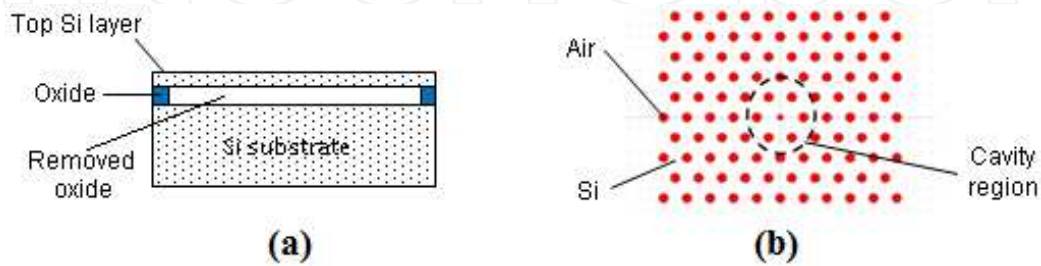


**Figure 6.** Cross section (a) and top view (b) of the PhC sensor based on air-bridge cavity.

The band gap map evidences a photonic band gap only for transverse electric (TE)-polarized mode in the microcavity. Under these conditions, the sensitivity has been estimated to be  $S=570\text{ nm/RIU}$ , higher than sensitivity evaluated in a simple SOI PhC-based sensor characterized by the same physical characteristics.

In the sensor presented above, the design of defect radius and slab thickness assumes a fundamental role for enhancing sensing performances. In fact, by changing the defect radius it is possible to obtain different band gap maps. Moreover, different defective states, and, consequently, different resonant conditions, can be properly introduced. For example, by increasing the defect hole radius a blue shift of resonant wavelength occurs, exhibiting a higher sensitivity. This effect is justified by the fact that a greater portion of localized field is distributed into the cavity region, resulting in a high overlapping between the resonant optical modes and the chemical/biochemical species to be sensed.

The slab thickness represents a key parameter because it influences performance parameters, i.e.,  $S_\lambda$  and  $Q$ -factor. In addition, also the field distribution and the energy bandgap are seriously affected by the slab thickness. In fact, for a thinner slab  $S_\lambda$  is larger and  $Q$ -factor is smaller because of less confinement and larger overlapping between the electric field intensity and the background. On the contrary, the resonant wavelength shifts to longer wavelengths by increasing the slab thickness.

A very interesting solution proposed for enhancing sensing performance consists in a PhC sensor based on RI sensing principle and characterized by an array of resonant microcavities.

The first device is embedded on monolithic silicon substrate of thickness  $t=0.55a=232.65\text{ nm}$  (Yang et al., 2011a). The 2D PhC is characterized by a triangular lattice of holes with lattice constant  $a=423\text{ nm}$  and air hole radius  $r=0.32a=135.36\text{ nm}$ . As shown in Fig. 7, the device

consists of a waveguide obtained by removing a row of air holes along the horizontal direction. Such waveguide guides light from the sensor input to the output. The cavity region is adjacent to the waveguide and it is realized by pulling outwards two holes in the opposite direction (parallel to the waveguide). In addition, radii of surrounding holes have been adjusted in order to optimize the cavity dimension. In particular, radius of left and right holes is set to be  $r_x = 0.25a$  and radius of top and bottom holes is  $r_y = 0.35a$ . The overall geometry is sketched in Fig. 7.

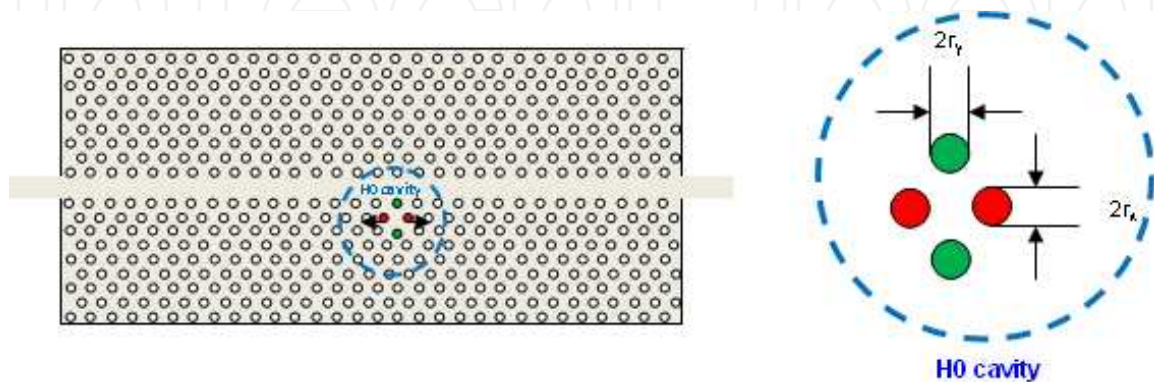


**Figure 7.** H0 cavity structure with the zoom of hole arrangement.

The hole shift represents a strategic design parameter. In fact, by varying the shift of cavity holes, the resonant wavelength of the transmission spectrum shifts, resulting in changes of the  $Q$ -factor, too. For the structure sketched in Fig. 7, it has been demonstrated that the optimal shift is  $s_x = 0.2a$ , because the maximum  $Q$ -factor is obtained at this value. In addition, the best set of radii has been set to  $r_x = 0.32a$  and  $r_y = 0.28a$ , in order to obtain a quality factor as high as  $Q = 2,761$ .

Another fundamental design parameter is the number of functionalized holes around the cavity region for mass sensitivity analysis. Initially, probe receptors are deposited on the inner hole surfaces near the cavity region. When target molecules are infiltrated into holes, the refractive index around the cavity area changes. This phenomenon is due to binding between probe molecules and target objects, resulting in a surface sensing.

It is convenient to introduce a new parameter known as mass sensitivity  $S_m$ , that illustrates the dependence of the resonant wavelength shift  $\Delta\lambda$  on the number of functionalized holes  $N$ :

$$S_m = \frac{\Delta\lambda}{N} \quad (6)$$

As expected, the sensitivity increases by decreasing the number of functionalized holes. The most sensitive holes to RI changes are the innermost ones in the  $y$  direction. Consequently, in order to optimize the sensing event, it is necessary to deposit a layer of probe molecules only on the surface of holes mentioned above.

In this way,  $n$  sensors are made in cascade, side-coupled with the same waveguide, allowing a multiple and parallel sensing. As sketched in Fig. 8, each H0-cavity is characterized by the same architecture with different sets of geometrical parameters. The transmission spectrum shows  $n$  different dips, each one independent from the others. When a binding event occurs, only the correspondent transmission dip is affected by a shift. This allows a multiple and simultaneous sensing of different chemical species.

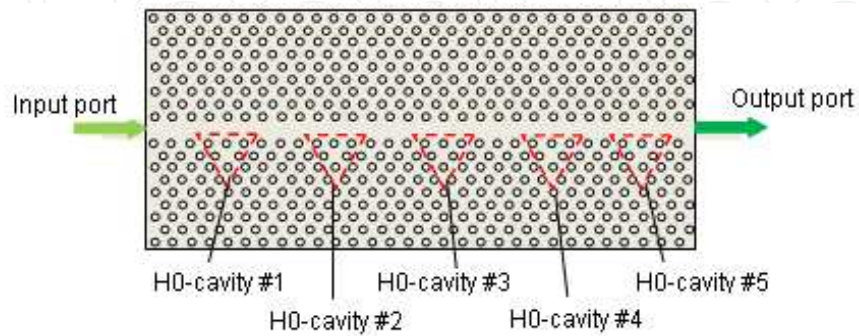


**Figure 8.** Array of H0 resonant cavities.

In conclusion, this sensor exhibits a wavelength sensitivity of 115.60 nm/RIU. In addition, the sensitivity can be also varied from 84.39 nm/RIU to 161.25 nm/RIU, by adjusting the number of functionalised holes from 2 to 28, respectively. The advantage of this architecture is represented by the low mass limit of detection achieved with small functionalized area, resulting in a good level of optical integration and large degree of multiplexed sensing in aqueous environment.

A RI-based PhC sensor based on the same architecture described above (i.e., a series of cascaded resonant cavities) has been proposed for simultaneous sensing of different species in aqueous environment (Mandal et al., 2009). The architecture consists of arrays of one-dimensional (1D) PhC resonators coupled to a single bus waveguide. Each cavity has a slightly different width with respect to the others, so that everyone can independently detect a different bio-molecular specie in response to changes of surrounding medium RI. The sensing mechanism occurs when bio molecules concentrated in the sensor cavity are captured by receptor molecules previously deposited on the sensor surface. Ring resonators have been designed in order to exhibit different and unique resonant wavelengths, so allowing multiplexed detection with a single waveguide. When target molecules are selectively captured by receptors, the dip in transmission spectrum shows a red shift. Analysis of the magnitude of this red shift provides quantitative information about concentration of target molecules in the sample and, consequently, about their bound mass.

The structure consists of a single mode silicon waveguide designed to be 450 nm wide and 250 nm tall, while resonators have been realized with the cavity region surrounded by 8 air holes at both sides with 200 nm in diameter, being the 1D lattice constant equal to 390 nm. The cavity area of the first sensor has been obtained by shifting outwards the innermost holes of 39 nm from the centre, as shown in Fig. 9.

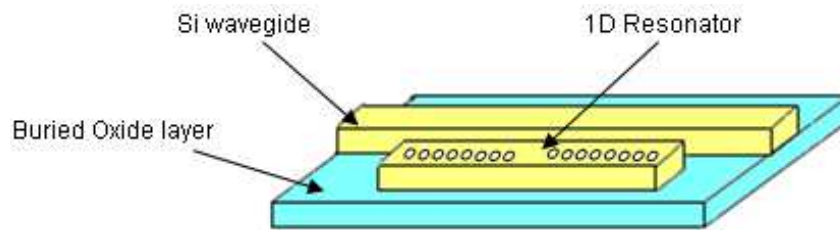


**Figure 9.** 1D-photonic crystal microcavity.

The architecture presented above has been adopted to detect different bio-molecules. The first configuration consists of five resonators, each one to be functionalized by a different probe. In particular, resonators functionalized with glutaraldehyde and streptavidin serve as control for non specific analyte adsorption. The other resonators functionalized with monoclonal antibodies are designed for monitoring and detecting *in-vivo* concentrations of interleukins 4, 6 and 8 (Mandal et al., 2009). The device can detect antibodies in a concentration range  $1 \mu\text{g/ml}$ – $1 \text{mg/ml}$ , suitable for clinical application and medical diagnostics, such as HIV test and drug screening.

The same architecture characterized by analogous arrangement of five resonators near the PhC waveguide, has been designed with a different number of functionalized holes rather than a different size of cavity regions (Mandal et al., 2008). Each resonator has been functionalized by a 50-nm-thick single stranded DNA (ssDNA) monolayer with refractive index  $n_{\text{ssDNA}} = 1.456$ . A detection event occurs when the complementary ssDNA hybridizes with the functionalized capture probes, forming a double stranded DNA (dsDNA). Moreover, the sensor sensitivity can be tuned by changing the number of functionalized holes, as reported in the expression below:

$$S_{\lambda} = \frac{\Delta\lambda}{\Delta m} = \frac{\Delta n}{\Delta m / A} \times \left[ \frac{\Delta\lambda}{\Delta n} \times \frac{1}{A} \right] \quad (7)$$

where  $\Delta n$  is the refractive index change due to the binding event,  $A$  is the functionalized area of the sensor,  $\Delta\lambda$  is the resonant wavelength shift and  $\Delta m$  is the mass of bound target. The sensor sensitivity increases by decreasing the number of functionalized holes  $N$ , as already demonstrated for sensor architectures previously analyzed. In this specific case, for only two functionalized holes a sensitivity as high as  $3.5 \text{ nm/fg}$  is achieved, while for sixteen holes the sensitivity drops to  $1 \text{ nm/fg}$ .

In this review on RI-based PhC integrated sensors we present also an innovative sensor able to detect *in-vivo*, single particles as small as viruses in aqueous and gaseous environment (Lee et al., 2008). The PhC sensor is characterized by an hexagonal array of cylindrical air holes embedded in a SOI wafer with a lattice constant  $a=400 \text{ nm}$  and a pore radius  $r=120 \text{ nm}$ . The radius of central hole is  $r_d=342.5 \text{ nm}$ , resulting in a band gap ranging from  $1440 \text{ nm}$  to  $1590 \text{ nm}$  for TE modes.

A latex sphere with a refractive index  $n = 1.45$  can be trapped into the central hole of the PhC, characterized by a bigger diameter compared to that of surrounding holes and to the diameter of the same sphere to be sensed. In this way, it is possible to detect the presence of the single particle trapped into the biggest hole by observing the resonant wavelength shift in the sensor transmission spectrum. In fact, when the sphere is trapped into the sensor cavity, the resonant peak characterized by a modest  $Q$ -factor around 2,000, is red shifted of about 4 nm. Moreover, the red shift proportionally increases as the latex sphere diameter increases, too. Finally, the sensor described until now represents a useful tool in medical and health applications for single molecule detection.

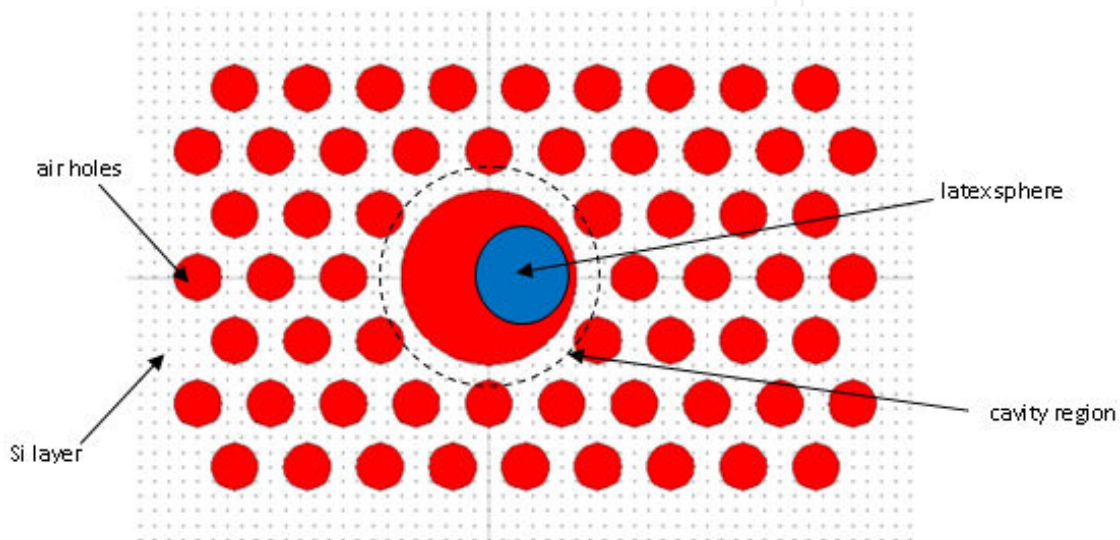


**Figure 10.** Top view of the PhC device with one latex sphere in the central defect of microcavity.

In several RI-based sensors the PhC waveguide directly acts as sensing element without designing any integrated microcavity, as previously analyzed in other sensor architectures. As before, a PhC waveguide is generally realized by introducing a line defect in the periodic planar structure. In such waveguide structures, only light at wavelengths outside the PhC bandgap can be guided. In particular, propagating modes are confined by Total Internal Reflection (TIR) along vertical direction and by the periodical structure laterally.

Performances of RI-based sensors can be quantified by monitoring the changes of cut-off wavelength ( $\lambda_{cutoff}$ ) as a function of the cover RI. In particular,  $\lambda_{cutoff}$  describes the maximum wavelength at which the optical mode can propagate in the PhC waveguide and it depends on the cover medium RI. Consequently, the sensor sensitivity can be defined as the ratio between changes of cut-off wavelength and changes of cover RI, as follows:

$$S = \frac{\partial T}{\partial n_c} = \frac{\Delta \lambda_{cutoff}}{\Delta n_c} \quad (8)$$

where  $T$  is the transmission spectrum,  $\Delta n_C$  is the cover medium RI change and  $\Delta\lambda_{cutoff}$  is the change of cut-off wavelength.

A RI-based PhC sensor has been proposed for detecting ssDNA, exhibiting a detection limit of 19.8 nM (García-Rupérez et al., 2010). This sensor, potentially able to detect very low analyte concentrations (e.g., proteins, bacteria, DNA) is fabricated in a SOI wafer with the silicon layer thickness of 250 nm and a 3- $\mu\text{m}$ -thick buried silicon dioxide.

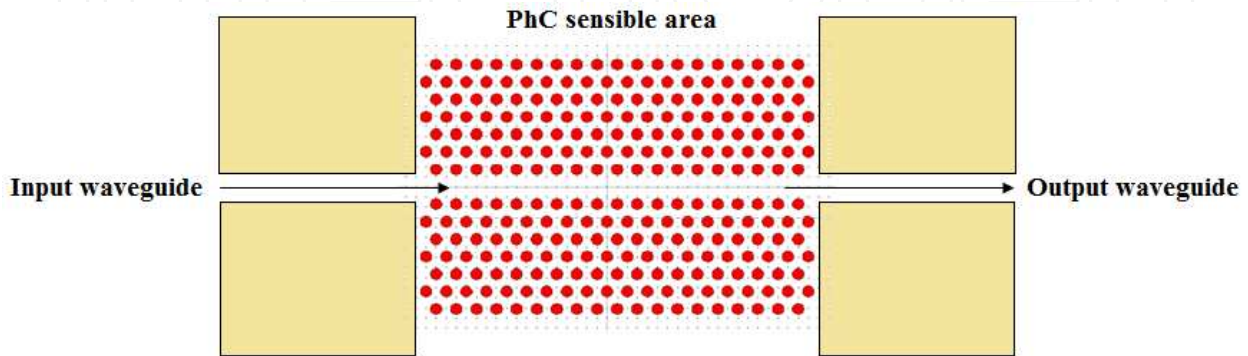


**Figure 11.** Schematic of the PhC-based DNA sensor characterized by input and output 500-nm-wide single mode waveguides.

The PhC lattice constant is  $a=390\text{ nm}$  and the hole radius is  $r=111\text{ nm}$ . Consequently, the structure exhibits a guided TE mode with its band edge located around  $\lambda=1550\text{ nm}$ . At the input and output of the PhC waveguide, light is coupled or collected by a 500-nm-wide single mode waveguide, as sketched in Fig. 11.

Sensing operative regime is performed by spectral peaks created by the excitation of multiple-k modes in the slow-wave regime near the band edge. In fact, changes of peak positions are continuously monitored, thus defining the sensor sensitivity according to Eq. (8).

The sensor has been tested with a complementary ssDNA solution bind to the ssDNA probe pre-deposited on the sensor surface. A peak shift of  $\Delta\lambda=47.1\text{ pm}$  corresponds to a DNA concentration of  $0.5\mu\text{M}$  in the complex sample.

An important parameter to be properly designed for increasing sensing performance in single line PhC waveguide sensor, is the radius of holes localized at both sides of the line defect (Bougriou et al., 2011). In this context, an integrated sensor based on a PhC waveguide has been proposed. The sensor architecture is characterized by circular air holes in silicon wafer, as sketched in Fig. 12. The triangular lattice structure has a lattice constant  $a=370\text{ nm}$  and hole radius  $r=120\text{ nm}$ . The waveguide is obtained by removing an entire row of holes in the horizontal direction, resulting in  $9.5\text{ }\mu\text{m}$  long PhC waveguide. In addition, 12 rows of holes are periodically distributed on each side of the line defect. The PhC sensor exhibits a large band gap between 1230 nm and 1720 nm for TE modes and a very small band gap for TM polarization.

Device sensitivity has been evaluated by monitoring the cut-off wavelength shift when the sensor, initially exposed to air cover ( $n_c=1$ ), is then covered by aqueous solution (i.e. de-ionized water with  $n_c=1.33$ ). Consequently, the cut-off wavelength shift is estimated to be 30 nm, due to cover RI change of 0.33 (1.33-1).

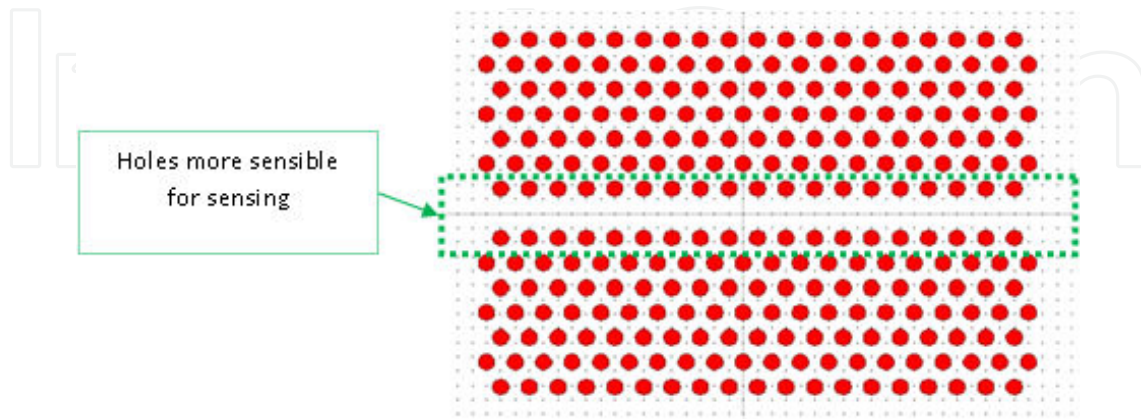


**Figure 12.** Photonic crystal waveguide sensor with sensible holes.

Sensor sensitivity can be improved by infiltrating the sample to be analyzed only in holes adjacent to the line defect. This arrangement produces a cut-off shift of 20 nm corresponding to a sensitivity of 60 nm/RIU. Experiments have shown that the sensitivity can be further increased by optimizing size holes near the line defect, which are more sensitive than outlying regions. In fact, by increasing the hole size, wavelength cut-off shift of 80 nm and sensitivity as high as  $S_\lambda = 240$  nm/RIU can be achieved, resulting in an improvement of about 62% with respect to the original sensor.

An RI-based sensor has been also proposed for gas sensing. In particular, the interaction between the slow light mode propagating in the structure and the gas infiltrated in it, is transduced by the waveguide effective refractive index changes, resulting in changes of slow light regime wavelength (Awad et al., 2011). This type of sensor has the advantage of improving the sensing performance because of the enhanced light-matter interaction. In addition, the selectivity of the sensor is ensured because the transmission spectrum changes its amplitude only when the gas is filled in the PhC structure.

As shown in Fig. 13, the sensor consists of an InP air bridge membrane configuration. In particular, a layer of air on the bottom and on the top of the 285-nm-thick PhC slab ensures the device symmetry. The PhC structure is embedded on the InP slab with triangular periodicity, lattice constant  $a=441$  nm and radius of air holes  $r=0.33a$ . The waveguide is obtained by removing an entire row of air holes.

Sensing performances have been estimated by exposing the sensor initially covered by air, to Argon ( $n = 1.000282$ ) and Helium ( $n = 1.000035$ ) gas, properly filled in the PhC waveguide. In particular, a shift of 0.6 nm has been detected in case of Helium filled in the waveguide and a shift of 0.05 nm in case of Argon. The sensor exhibits a good tolerance from environmental

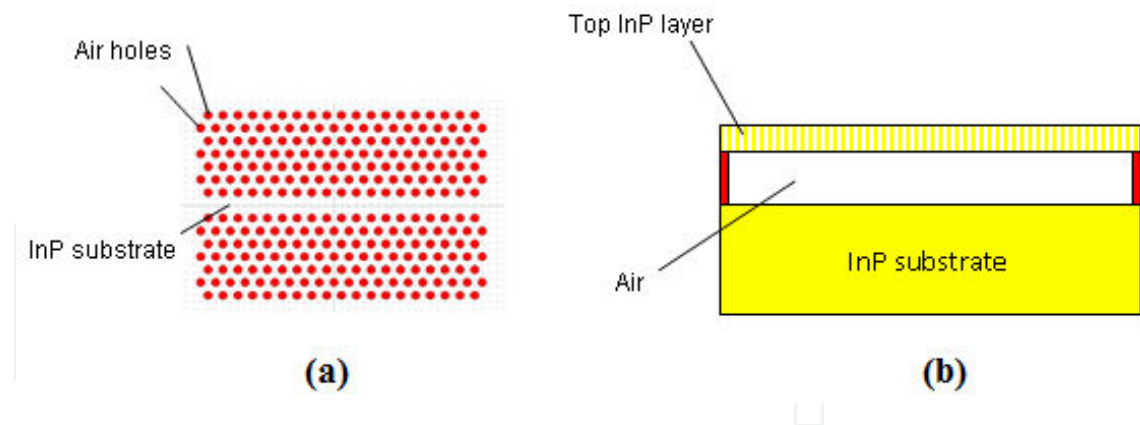


**Figure 13.** a) Top and (b) cross-sectional view of photonic crystal waveguide sensor for gas sensing.

perturbations and it is able to detect all gases characterized by refractive indices similar to Argon and Helium ones, with the exception of those whose refractive indices are very close to air RI (i.e.,  $n_{Air} = 1$ ).

In conclusion, PhC-based sensors integrated in interferometer architectures have been reviewed. Generally, sensing principle characterizing interferometer architectures are based on phase-shift measurement. In particular, if a perturbation occurs only on one arm of the interferometer, the output signal differs from the input signal, showing a variation of its phase or amplitude. In Mach Zehnder configuration it is possible to quantify the amount of phase shift on the active arm by tracking the signal output intensity. The perturbation mentioned above can be associated to the change of cover refractive index in one arm of the MZI, due to the presence of analytes in the sample. This phenomenon can be described by the following relation:

$$\Delta\varphi = \Delta\beta L = \frac{2\pi}{\lambda} \Delta n L \quad (9)$$

where  $\Delta n$  is the refractive index variation,  $L$  is the length of the waveguide and  $\lambda$  is the wavelength.

As sketched in Fig. 14, a MZI-based sensor with slot PhC waveguide has been fabricated and experimentally characterized (Chen et al., 2008). The sensor is composed by PhC waveguides in both active and reference arms, rib waveguides for sensor input and output, Y-junctions, electrodes and electrode pads. In particular, PhC waveguides are realized by removing a single row of air hole in a silicon slab. The device is fabricated on a SOI wafer, in which the thickness of the silicon core layer is  $t = 215 \text{ nm}$ , the top cladding medium is air and the bottom layer is a 2- $\mu\text{m}$ -thick buried oxide layer. In the silicon slab, the holes are arranged by hexagonal cells with lattice constant  $a = 400 \text{ nm}$  resulting in air hole diameter  $d = 0.53a$ .

For sensor applications, it is possible to induce localized RI changes by filling the waveguide region with gas- or liquid-phase analyte materials. By this way, the output signal intensity can be varied because of the conjunction effect of static driving voltage supported through

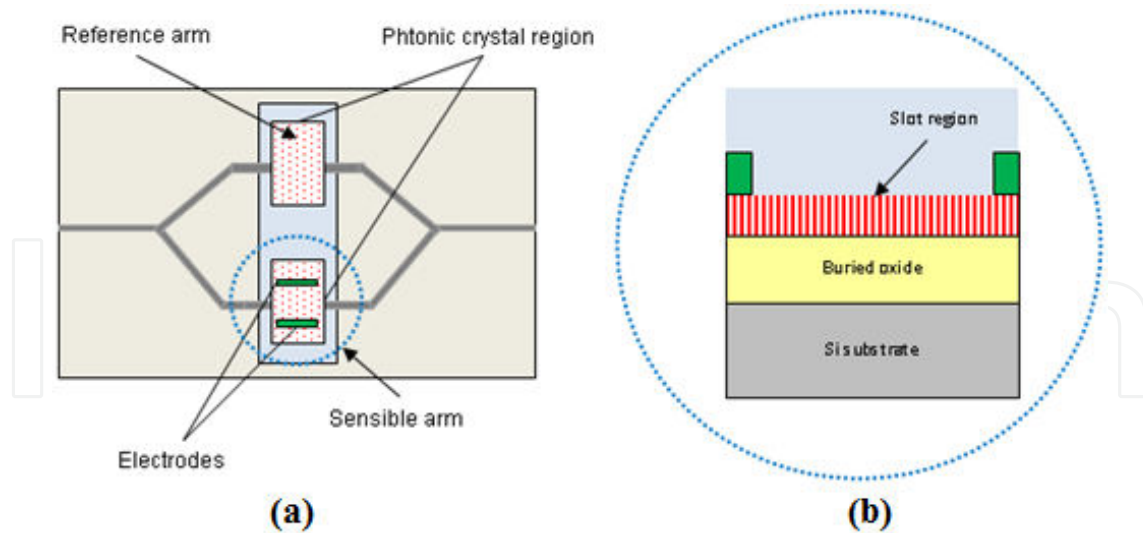


**Figure 14.** MZI with slot Photonic Crystal waveguide (a) and cross-sectional view (b).

electrodes on the sensor arms and cover RI changes. Finally, experimental comparison evidences how silicon slot PhC waveguide provides 30 times effective index change compared with conventional silicon slotted strip waveguide.

A sensor which combines the optical power splitting characteristics of multi-mode interference (MMI) power splitter and transmission drop resonance characteristics of multiple PhC microcavities arrays, has been recently investigated and proposed (Zou et al., 2012). The device, sketched in Fig. 15, is fabricated on a SOI platform and consists of a 1x4 MMI optical power splitter which splits the input light from a ridge waveguide into four output channels. The MMI has a length and a width of 123  $\mu\text{m}$  and 16  $\mu\text{m}$ , respectively. The input waveguide is 2.5- $\mu\text{m}$ -width and outputs are separated by 1.5  $\mu\text{m}$ . PhC waveguides are line defects with uniform lattice constant  $a = 400 \text{ nm}$  and diameter holes  $d = 0.54a$  which is embedded on a silicon slab thickness  $t = 0.58a = 232 \text{ nm}$ .

On arms #1 to #3, the edge air holes on the axis of PhC microcavity are shifted outward in the horizontal direction by a distance equal to  $0.15a$ . On the arm #4, two microcavities spaced of 50  $\mu\text{m}$ , are designed as L13 type. In the first one, edge-air holes are shifted inward by  $0.15a$ , in the second microcavity edge-air holes are shifted outward by  $0.15a$  resulting in zero cross talk.

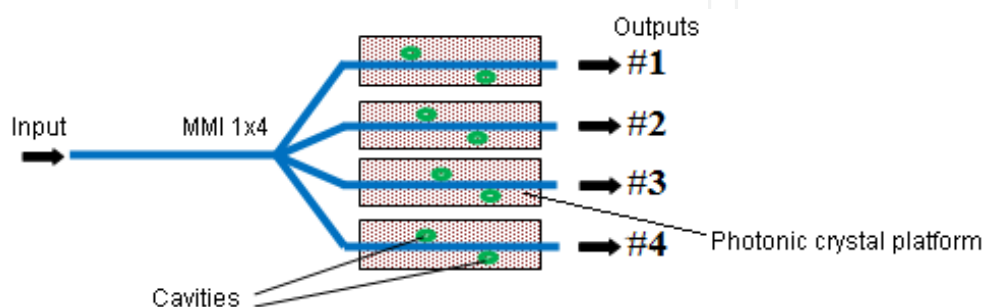


**Figure 15.** Schematic of 1x4 MMI device.

Each microcavity is coated with different receptor biomolecules, each responsive to its specific conjugate. In fact, by introducing into the sensible area 60  $\mu\text{l}$  of 600 nM of goat anti-rabbit IgG Abs dissolved in PBS, only transmission spectrum of arm #2 changes, showing a resonant wavelength shift. In fact, the arm #2 is printed with a specific conjugate rabbit anti-goat IgG Abs. The arm #4 operates similarly while any shift is observed in remaining arms because arm #1 and #3 are printed with human IL-10 Abs, and arm #4 in the second microcavity is coated with BSA. Consequently, by changing the sample solution, thus by introducing 60  $\mu\text{l}$  of 600 nM of rat anti-human IL-10 Abs dissolved in PBS, only one resonance wavelength shift is observed in arm #1. Finally, the sensor is immune to environmental changes and allows multiple detection, being very suitable for high throughput-screening.

## 2.2. Photonic crystal sensors based on optical adsorption

A lot of gas and liquid molecules absorb radiation in near- and mid-infrared, being spectroscopically detectable. In particular, when the wavelength of the optical signal matches the natural frequencies or resonances of the irradiated gas or molecule, the energy states of vibrating atoms change in discrete steps. The resonance frequencies or wavelengths depend on the number and mass of atoms in molecules as well as the number and strengths of chemical bonds. If the chemical structure of the molecules is complex, then a range of resonant vibrations characterize the optical absorption of molecules.

Based on these simple principles, the infrared (IR) spectroscopy is the simplest and the most reliable spectroscopic and sensing technique. In particular, the absorption spectroscopy is based on the Beer-Lambert law, defined as follows:

$$I = I_0 \exp(-\alpha L), \quad \alpha = \eta C \quad (10)$$

where  $I_0$  is the intensity of the incident light,  $\alpha$  is the absorption coefficient of the chemical specie being linearly dependent to the analyte concentration  $C$  via the molar absorptivity  $\eta$ , and  $L$  is the interaction length.

In this context, a photonic sensor based on a PhC slot waveguide has been proposed (Chakravarty et al., 2011a). The PhC waveguide is obtained by removing a single row of air holes from the input to the output of the device, resulting in a line defect with uniform lattice constant  $a$ . The device is designed for xylene sensing. Consequently the sensing platform is coated with a hydrophobic  $\sim 0.8$ - $\mu\text{m}$ -thick film of poly-dimethyl siloxane (PDMS). In this way, sensor selectivity is enhanced because adsorption of xylene is ensured by the functionalized coating and the adsorption of water is inhibited by the hydrophobic properties of PDMS. The width of PhC waveguide is  $1.3 \times \sqrt{3}a$ , the hole radius is  $r = 0.25a$ , the slot width  $w = 0.2a$  and the waveguide length is  $L = 300 \mu\text{m}$ . The slow light guided mode propagates at normalized frequency  $a/\lambda = 0.275$  and at this wavelength the constant lattice is set to be  $a = 461 \text{ nm}$ .

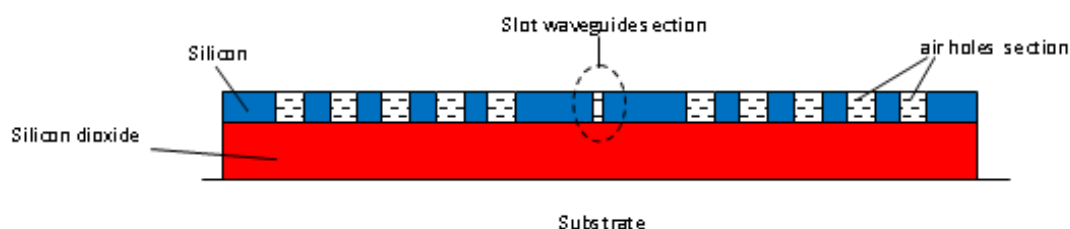


**Figure 16.** Cross section of PhC slot waveguide.

The whole device, sketched in Fig. 16, has been fabricated on SOI wafer with 230-nm-thick top layer and 3- $\mu\text{m}$ -thick buried oxide. The sensing mechanism takes place by introducing analyte in the device sensible area through tygon tubes.

The absorption spectrum of xylene is characterized by three absorption peaks approximately centered at 1674 nm, 1697 nm and 1725 nm, being the latter peak characterized by a very small intensity. Moreover, when a xylene concentration dissolved in deionized (DI) water is introduced into the device, the intensity of the strongest absorbance peak at 1697 nm changes linearly for small concentrations of xylene (from 100 ppb to 1 ppm), in agreement with the Beer-Lambert law. At higher concentrations the absorbance curve deviates from linearity because the PDMS film reaches saturation and reduces its absorption capacity.

An analogous architecture with the same values of geometrical parameters is used for methane detection (Chakravarty et al., 2011b). The major absorption peak of methane occurs at 1.665  $\mu\text{m}$ .

The experimental response of the sensor proposed follows the linear Beer-Lambert function for low concentrations of methane in nitrogen, being 100 ppm the lowest detectable methane concentration, and exhibits a deviation for higher concentrations, as previously analyzed in case of xylene detection.

Another similar sensor characterized by slow light mode propagation has been proposed for detection of hazardous gases and analytes in aqueous environment (Thévenaz et al., 2012). The PhC waveguide consists of a 180-nm-thick GaInP slab with a triangular lattice of air holes having a lattice constant of 486 nm and a defect line. In various experiments, the size of the first row of holes has been changed in order to firstly modify dispersion properties of the device and secondly to optimize sensing performance. In the first case, the hole size has been increased from 204 nm to 233 nm, in the second case from 224 nm to 253 nm. These two different geometrical arrangements influence the group refractive index  $n_g$ . In fact, when a TE-polarized mode is launched in the sensor the group index is measured to be  $n_g = 4.9$  and  $n_g = 6.7$  for the first and second configuration, respectively. In case of transverse magnetic-(TM)-polarized mode launched into the sensor,  $n_g$  remains the same in both configurations, to be equal to 1.5.

The sensor is placed in a gas chamber hermetically closed, filled with acetylene gas at 50 torr. In this way, the absorption coefficient is maximized and the linewidth of the absorption peak is kept narrow. Finally, the sensor confirms a linear dependence of molecular absorption on the group index and evidences how the distribution of the electric field is a very important

parameter in gas-sensing measurements. In fact, by considering TM-polarized mode propagating in the sensor, a stronger optical absorption is achieved compared with that obtained when TE-polarized mode propagates in the same sensor. This effect, is due to fact that in TM polarization the electric field inside the lower-index slab material is increased by discontinuity at dielectric interface.

Theoretically, it is possible to define the absorption coefficient as the ratio between the electric field obtained by coupling optical wave and electric dipole and the Poynting vector. An analytical expression for  $\alpha$  is reported below:

$$\alpha \approx \frac{\int \text{Im}[\varepsilon] |E|^2 dV / 2}{\text{Re} \left[ \int_A E \times H^* dA \right]} \quad (11)$$

where  $H$  is the magnetic field,  $\varepsilon$  is the complex electric permittivity and  $Re$  and  $Im$  denote the real and imaginary part of a complex number, respectively. In conclusion, the enhanced overlapping between electric field intensity and molecule to be sensed evidences a decisive influence on the absorption enhancement, thus in sensing performance.

Finally, a PhC sensor based on infrared absorption has been proposed for azote oxide ( $\text{NO}_2$ ) detection (Maulina et al., 2011). The sensor consists of 1D PhC characterized by two different defects. In addition, by changing the refractive index and thickness of both defects, it is possible to tune the position of photonic pass band (PBB) in the PhC band gap.

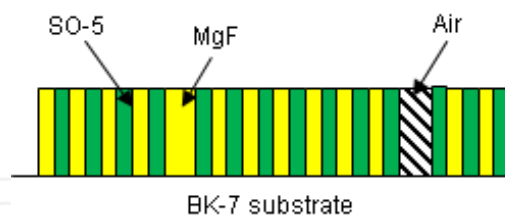


**Figure 17.** 1D-PhC with two defects for  $\text{NO}_2$  sensing.

The two defects are named as regulator and receptor. Changes in the regulator defect influence the wavelength of the transmission spectrum, while changes in receptor defect induce variations in transmittance value. In particular, as plotted in Figure 17, the sensor consists of a first defect sandwiched between 4 and 6 periodic cells, and the second adjacent defect sandwiched between 6 and 2 cells. A cell is characterized by two alternate layers being the first layer (i.e., OS-5) characterized by a high refractive index  $n = 2.1$ , and the second one magnesium fluoride ( $\text{MgF}_2$ ) with the lower refractive index,  $n = 1.38$ . In addition, the first defect is OS-5 having twice the thickness of the other layers. The second defect is a void (low air refractive index  $n = 1$ ) to be filled with the sample to be detected. Finally, the whole structure is embedded

on a layer of glass material borosilicate crown, known as BK-7 whose refractive index is  $n = 1.52$ . Experimental results have been performed by absorbing  $\text{NO}_2$  in air, combining Beer-Lambert's law and PBB phenomena. The PBB spectra change with respect to different concentrations of absorbed  $\text{NO}_2$  gas. Results of spectroscopic measurements evidence a linear rise of transmittance value with increasing the gas concentrations. Finally, the sensor presented until now exhibits an efficiency up to 99 %.

### 2.3. Integrated photonic crystal sensors based on non linear effect

Recent studies have shown how new PhC sensors based on non linear effects represent a new and intriguing approach for advanced sensing applications. Actually, the main non linear effects investigated in these structures are Kerr nonlinearities (Van Driel, 2003), Raman effect and harmonic generation.

In this section, an original sensor is proposed, consisting in a PhC microcavity in which the Raman effect related to the vibrational excitations mode in silica is excited. By considering the quantum mechanical approach, a photon of the incident field (i.e., the pump wave) is scattered by a molecule of the medium in which the field propagates, resulting in the generation of a photon of lower energy (i.e., the Stokes wave). At the same time, the residual energy is absorbed by molecules via phonons. The Raman shift is then the frequency difference between the incident wave and the scattered one (Stokes wave) in a stimulated Raman interaction.

The device proposed in this section, is based on a PhC cavity fabricated on a 220 nm SOI wafer (Van Leest et al., 2012). Air holes in the silicon slab are arranged in hexagonal cells with lattice constant  $a = 430 \text{ nm}$  and radius of air holes  $r = 0.3a = 129 \text{ nm}$ .

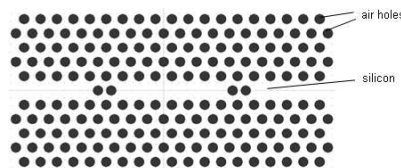


**Figure 18.** Schematic of L6 cavity to generate Raman effect.

The device proposed is characterized by a L6 PhC cavity, i.e. a PhC structure without six central air holes, as sketched in Fig. 18 above.

A resonant cavity with the overall length  $L_{cav} = 2.9 \mu\text{m}$  is obtained by shifting outward the inner holes along horizontal direction by a distance equal to  $0.2 \cdot a = 0.086 \mu\text{m}$ . Mathematical modeling of the device suggests this design approach as fundamental in order to ensure the generation of Stokes wave into the cavity, away from the resonant wavelength of about 15,6 THz. This wavelength shift due to pump wave and resonant Stokes wavelength generated into the cavity, is typical for silica.

In conclusion, the sensor investigated evidences intriguing potentialities and sensing performance of new class of PhC sensors based on non linear effect (i.e., Raman effect). In

particular, such sensors are expected to be able to detect single particle in aqueous solutions, with very small dimensions comparable to that of virus or proteins.

Several research efforts are still being done in order to comprehend how to employ non linear effects for sensing applications in PhC sensors fabricated on SOI technological platform.

#### 2.4. Opto-mechanical sensors based on PhC

In this section, PhC-based sensors designed for pressure, force, strain and torsion sensing, are discussed. The sensing principle consists in monitoring variations of optical characteristics induced by the physical deformation of the PhC-based device.

In this context, a force and strain sensor is sketched in Fig. 19 (Li et al., 2011).

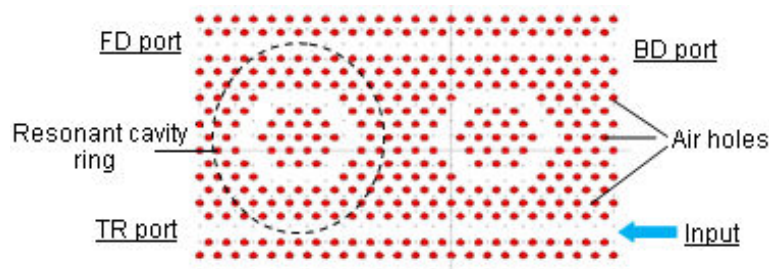


**Figure 19.** Schematic of DNR channel drop filter.

The architecture presented above is a typical dual-nanoring (DNR) channel drop filter on 2D photonic crystal with hexagonal lattice. A silicon PhC crystal slab of 220 nm thickness is released on a SOI substrate and the ratio between radius of air holes and lattice constant is set to be  $r/a=0.292$ .

The nanoring is obtained by removing localized air holes to form an hexagonal defect. The dual-nanoring is made by two aligned nanorings with a centre-to-centre distance  $d=11a$ . The structure is sandwiched between two waveguides, so that it is possible to identify four ports in the PhC platform. The first one acts as input port (red arrow) and the other ones are used for transmission (TR) and forward (FD) or backward drop (BD), indicated in Fig. 19 as TR port, FD port and BD port, respectively.

The device characterized by PhC single-nanoring structure shows a photonic band gap map for TM modes, characterized by a band gap in the range of normalized frequency extended from 0.26 to 0.33. The corresponding band gap wavelength ranges from 1242 nm to 1577 nm and a resonant peak displayed in BD port is located at 1553.6 nm revealing a  $Q$ -factor of 3,884, while FD and TR ports reveal a spectral dip at the same wavelength mentioned above.

Simulations evidence that two rings are always phase-matched and their resonances are not independently. In fact, Li et al. have demonstrated that the wavelength of the resonant peak at the BD port is strongly dependent on the ring size and separation distance  $d$  between two rings. Consequently, when physical structure is deformed, a variation of the resonant wave-

length can be detected. The application of an external force to the device induces a strain linearly proportional to the applied force located at the junction between cantilever and SOI substrate.

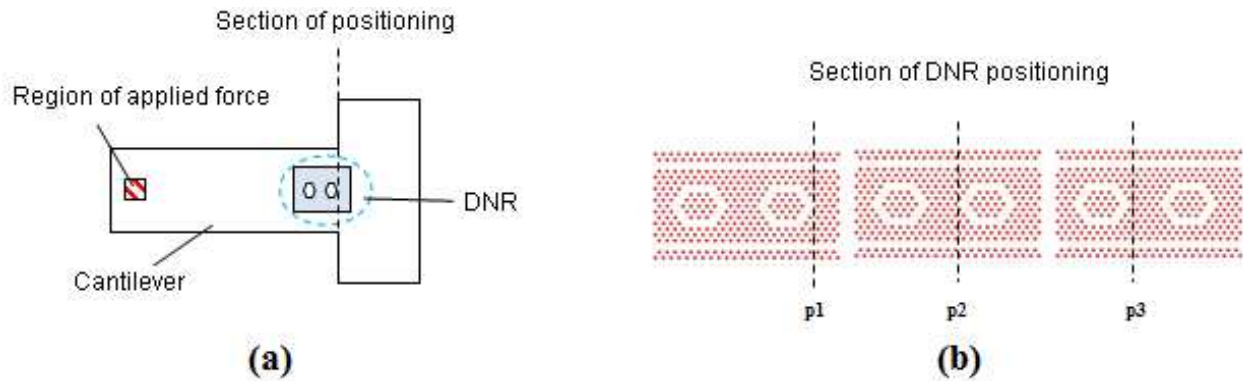


**Figure 20.** Cantilever architecture (a) and different positioning of DNR on cantilever (b).

In particular, the stronger the applied force, thus the strain induced to the sensor, the bigger the red shift of the resonant wavelength to be detected. As sketched in Fig. 20, three different configurations are adopted by moving the DNR resonator on the cantilever and three different correspondent sensor responses are obtained. For example, in cantilever labelled as type p1, the resonant peak shifts from 1553.6 nm to 1554.9 nm, corresponding to a force variation ranging from 0 to 400 nN. In this configuration, as the load force approaches to 500 nN, the output signal intensity at the BD port is lightly reduced, while the signal intensity at the FD port increases. Consequently the signal intensity at the TR port is also increased. The device exhibits a degraded resonant behaviour due to deformed DNR resonator.

The cantilever labelled as type 2p, maintains the channel drop mechanism up to the load force of 700 nN before losing its resonant behaviour. In the last configuration indicated as type p3, only the second ring is kept within the deformation region and the sensitivity of the DNR is reduced. In fact, a less range of load force is detected through this type of cantilever. The BD behaviour is degraded in case of applied force higher than 100 nN.

A PhC micro-pressure sensor has been fabricated and characterized (Bakhtazad et al., 2010). The device is based on an air-bridged line-defect silicon slab PhC waveguide, as sketched in Fig. 21.

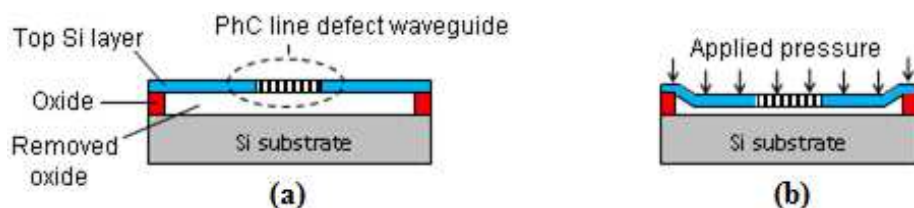


**Figure 21.** Sensor at rest (a) and sensor with applied pressure (b).

The device is fabricated in SOI technology. In this structure the bridge is obtained by removing a portion of buried oxide layer of 1000 nm thickness, while the top silicon layer is 320-nm-thick.

The PhC structure has hexagonal lattice with lattice constant  $a=430\text{ nm}$ , diameter holes  $d=300\text{ nm}$ . A waveguide is embedded by removing a row of holes in  $\Gamma K$  direction. Two 700-nm-thick channel waveguides are placed at input and output section in order to ensure an efficient light coupling. In case of TM polarization, the structure shows a band gap with its centre at about 1550 nm.

The sensor operation is based on the optical field profile changes to the proximity of surrounding material induced by the applied pressure on the top of the sensor. Consequently, changes in the transmission spectrum are directly linked to the magnitude of the applied force. To this purpose, it is possible to define the device sensitivity as follows:

$$S = \frac{\delta T}{\delta P} = \frac{\delta T}{\delta h} \times \frac{\delta h}{\delta P} \quad (12)$$

where  $T$  is the optical transmittance,  $P$  the applied pressure and  $h$  is the photonic crystal height over the substrate. The best total sensitivity obtained is  $S = 0.039$  (%/MPa) under 1MPa uniform pressure, i.e. a maximum displacement at centre of the rectangular platform of 78 pm.

A PhC optical cavity has been designed for detecting torsion or flexure induced by external magnetic couple excitations (Wu et al., 2012). The design of this sensor is optimized to support low effective mass torsional and flexural mechanical modes. The sensor is characterized by a PhC opto-mechanical cavity in which the central element results to be suspended. This type of sensors have been proposed for magnetic applications and are suitable for probing nano-magnetic torques.

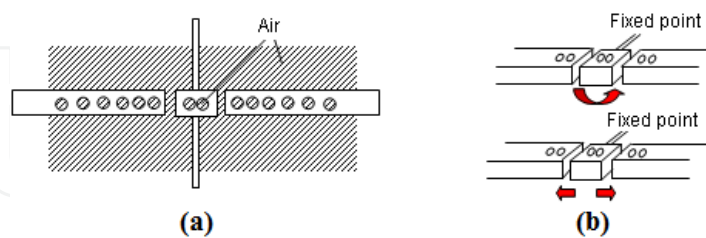


**Figure 22.** Schematic of the torsion PhC-based sensor (a) and operative configurations (b): right torsional (top) and flexural (bottom) movements of central sensor element.

As sketched in Fig. 22, the overall structure is characterized by air holes with radius  $r=145\text{ nm}$ , patterned in a free standing silicon nanowire with refractive index  $n=3.5$ , thickness  $t=250\text{ nm}$  and width  $w=600\text{ nm}$ . The hole spacing varies quadratically over six periods, ranging from  $a_c=350\text{ nm}$  to  $a_0=450\text{ nm}$ . The suspended element is disconnected from the two arms of the sensor by a gap of size  $d=0.58a_0$ . Central position is defined as  $a_2'=1.12 a_2$  where  $a_2$

is the nominal spacing between the first and second hole of the uncut structure. The gap reduces the maximum value of device  $Q$ -factor. Moreover, the structure can support a  $Q$ -factor higher than  $10^4$  by tuning gap size,  $d$  parameter and gap position.

In presence of an external magnetic field, torsional and flexural resonance may be excited by magnetic moment from nanomagnetic materials attached to the nanocavity paddle. These magnetic resonance affects the suspended central element in the PhC cavity, inducing changes of optical properties. Experimental results show higher  $Q$ -factor values and lower effective mechanical mass ( $\sim 100$  fg).

## 2.5. Advances in PhC-based sensors: Materials and technologies

In this section, techniques commonly used for PhC fabrication, are briefly discussed. The fabrication of these devices requires a series of technological steps which establish the effective physical characteristics of the photonic crystal. In fact, periodicity, depth and radii of PhC holes can be precisely controlled during technological processes, strongly influencing real performances of the resulting PhC-based sensor. In particular, the geometrical arrangement strongly affects the photonic crystal band gap map, influencing optical mode propagation properties.

In the following, an example of photonic crystal device fabrication is described. In particular, when the photonic crystal is embedded on SOI chip, the first step generally consists in cleaning the device surface with nitric acid in order to remove organic residuals. Consequently, a positive electron beam (e-beam) resist is spun on the top surface of the SOI chip. The photonic crystal is patterned using an e-beam lithography system operating at 100 keV. The resist is developed with a microchem 1:3 methyl-isobutyl ketone:isopropanol (MIBK:IPA) solution for 30 s followed by a 10 s IPA rinse. Successively, the exposed areas are then etched using inductively coupled plasma (ICP) dry etching system or Chlorine based ICP. The remaining resist can be dissolved in a dilute 100:1 HF solution.

The top of device is often covered with a layer of polydimethylsiloxane (PDMS) that is realized by using a soft lithography technique.

Micro fluidic channels, widely used in chemical and biochemical PhC-based sensing architectures, require precise fabrication steps. Initially, a mold for the channels is created by using a 4-inch pure silicon wafer. A 1- $\mu\text{m}$ -thick UV resist layer is spun on the top of silicon, followed by Near-UV lithography for writing the desired patterns of fluidic channels. Pattern-transfer is done by reactive ion etching (RIE) and a depth of approximately 30  $\mu\text{m}$  can be realized by conventional etching. In conclusion, a PDMS layer is poured onto the silicon mold in order to create flow channels.

The fabrication steps can differ for various devices depending on the materials employed, thus the technological platform. For example, a guiding  $\text{SiN}_x$  layer can be deposited on the substrate by either Plasma Enhanced Chemical Vapor Deposition (PECVD) or Low Pressure Chemical Vapor Deposition (LPCVD) techniques in order to optimize the film uniformity. This layer can be patterned in a photonic crystal structure using either optical or e-beam lithography. The first lithography technique is often used for large area array, the second one is preferred for

much smaller device dimensions, being characterized by an higher resolution. The e-beam is well-suited for flexible PhC lattice design. The pattern is transferred from the resist to the  $\text{SiN}_x$  layer using Fluorine-based dry etching.

Recently, several technological processes have been investigated and tested for fabrication of 3D PhC devices. This new class of devices is not popular as 2D PhCs, because the planar technology is more established and applications of 2D PhCs are well established in optical telecommunication, signal-processing and sensing.

In this context, the first sensor proposed is a PhC hydrogel for sensing of highly toxic mercury ion ( $\text{Hg}^{2+}$ ) in water (Arunbabu et al., 2011). The detection of  $\text{Hg}^{2+}$  concentration is due to diffraction of visible light from polymerized crystalline colloidal array (PCCA) which consists of highly charged polystyrene particles which are polymerized within the polyacrylamide hydrogel (named crystalline colloidal array or CCA). Different concentrations of analytes in the 3D PhC change the volume of hydrogel resulting in an alteration of the lattice spacing of CCA and, consequently, in a shift of the diffraction wavelength of light. Therefore, the concentration of analytes can be extracted from the wavelength of diffracted light by PCCA. In particular, this sensor employs an urease immobilized PCCA based sensing material for determination of  $\text{Hg}^{2+}$ . In fact, the presence of  $\text{Hg}^{2+}$  in a solution in contact with the PCCA inhibits the urea hydrolysis and suppresses the normal production of  $\text{NH}_4^+$  and  $\text{HCO}_3^-$ . The optical result is a red shift diffraction which increases linearly for low concentration of  $\text{Hg}^{2+}$  and devices to linearity for higher concentration of  $\text{Hg}^{2+}$ .

The sensor shows reversibility and LOD as low as 1 ppb, i.e., 1  $\mu\text{g/L}$ . In conclusion, the sensor can be used with the same physical principle for detection of  $\text{Ag}^+$  and  $\text{Cu}^{2+}$  ions which are, as  $\text{Hg}^{2+}$ , the principal inhibitor of urease.

A mechanically robust and highly sensitive sensor, with short response time, characterized by a planar defect in the 3D macroporous array of pH-sensitive hydrogel poly (methacrylic acid) (PMMA), has been proposed for pH detection (Griffete et al., 2011). Two different configurations of the structure fabricated by a Langimur-Blodgett technique and characterized by hexagonal arrangement of spheres have been designed. In particular, one structure is a defect-free (DF) colloidal crystal made from 10 layers of 280 nm diameter particles. The other one is a planar defect-containing (DC) colloidal crystal which consists of a layer of silica particles of 390 nm diameter between two sections of 5 layers of particles of 240 nm diameter. As previously analyzed in case of 2D planar PhC sensors, the defective layer in 3D technology also introduces a change into the band gap map, influencing the optical properties of the device (see Fig. 23).

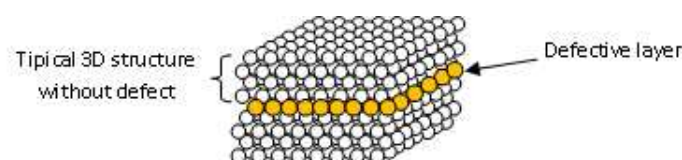


**Figure 23.** 3D-PhC with defected layer.

In both structures, by increasing the pH of the complex sample a red shift of the diffraction peak can be observed due to the ionization of the ionic gel. The diffraction red shift occurs after the gel is swollen. The presence of defect in the 3D PhC structure enhances both sensitivity and response time of the PhC sensor. In fact, the device characterized by the defect shows a red-shift of  $\Delta\lambda = 60 \text{ nm}$  that is greater than the wavelength shift  $\Delta\lambda = 40 \text{ nm}$  obtained with the defect-free device and estimated for the same pH concentration.

A different architecture used for pH sensing (Jiang et al., 2012) is based on poly(vinyl alcohol) (PVA)/poly(acrylic acid) (PAA) photonic crystal materials. This sensor exhibits good durability and adjustability. The pH response is monitored by diffraction wavelength shift. A solvent-assisted method is used to physically cross-link a thermo-reversible PVA hydrogel around CCA and form a gelated crystalline colloidal array photonic crystal material (GCCA). Glutaraldehyde is used to chemically cross-link the PVA hydrogel in order to avoid the collapse of cross-linked GCCA during the procedure for the introduction of environmentally sensitive components. It has been demonstrated that the sensing is better for high concentration of glutaraldehyde solution, because the high cross-link density improves equilibrium hydrogel volume needed for the diffraction shift measuring. The modified Bragg's law reported in Eq. (13), regulates the phenomenon mentioned above:

$$m\lambda = \sqrt{\frac{8}{3}} D \left( \sum_i n_i^2 V_i - \sin^2 \theta \right)^{\frac{1}{2}} \quad (13)$$

where  $D$  is the center-to-center distance between the nearest spheres,  $n_i$  and  $V_i$  are the refractive index and volume of each component, respectively, and  $\theta$  is the angle between the incident light and the sample normal. As pH increases the hydrogel absorbs water and swell. The center-to-center distance also increases and a red shift of the diffraction peak is generated. The sensor exhibits a wavelength shift of  $\Delta\lambda = 96 \text{ nm}$  when a solution of pH 7.6 is concentrated in cover medium for 30 min, being the same sensor initially exposed to a solution of pH = 4.8.

In conclusion, a photonic sensor consisting of a glass substrate and a three dimensional photonic crystal realized by using nanoparticles and poly(dimethylsiloxane) (PDMS) elastomer has been investigated (Endo et al., 2007). The PhC is generated by infiltrating the opaline lattice of particles with a liquid prepolymer to PMDS in voids. Subsequently the material is thermal cured.

Even in this case, the physical sensing is governed by the Bragg's law that can be written in terms of spacing between planes of crystal ( $d_{111}$ ) as follows:

$$m\lambda = 2d_{111} \left( n_{eff}^2 - \sin^2 \theta \right)^{\frac{1}{2}} \quad (14)$$

where  $m$  is the order of diffraction and  $n_{eff}$  is the mean refractive index of the crystalline lattice.

The first step for the sensor fabrication consists in drying aqueous dispersions of polystyrene (PS) nanoparticles (with 202 nm-diameter) on the glass substrate. After the dry-up process when the PS nanoparticles are spatially ordered, a PMDS solution without any air bubbles is distributed on the top of PhC and all voids between the PS nanoparticles are totally filled. The PDMS is first cured at room temperature, then it is baked at 60°C for 1 hour.

The sensor obtained, exhibits a Bragg reflection peak at 552 nm. When a non-polar organic solvent such as xylene is in contact with the structure, it is possible to see a color change of 3D structure from green to red. The shift increases when concentration of solvent in the solution increases. In addition, the detection limit of this optical chemical sensor is found to be dependent on the polarities of the solvents.

### 3. Photonic crystal fiber sensors

Photonic crystal fibers (PCFs), also named as micro-structured optical fibers (MOFs), represent nowadays a new and intriguing typology of optical fibers suitable for sensing applications such as measurement of strain, refractive index, pressure, temperature, magnetic field, to name a few. PCF-based sensors are characterized by high sensitivity, small size, robustness, flexibility and ability for remote sensing. Other advantages concern with the possibility to be used even in the presence of unfavorable environmental conditions such as noise, strong electromagnetic fields, high voltages, nuclear radiation, for explosive or chemically corrosive media, and at high temperatures.

Substantially, PCFs are fused-silica optical fibers characterized by a hollow or silica core surrounding by a regular pattern of voids running along the fiber axis, as sketched in Fig. 30 below.

In particular, it is possible to appreciate the difference among PCFs, as in Fig. 24(a-b), with respect to conventional single mode fibers (SMFs), as in Fig. 24(c). In particular, propagation properties in conventional optical fibers and PCFs can be tuned by properly designing geometrical parameters, such as the hole diameter indicated with  $h$ , the fiber core diameter  $d$ , the pitch  $x$  (i.e., the distance between the center points of two consecutive holes), the fiber length  $L$  and, obviously, materials.

In PCFs, light can be guided by two different mechanisms, i.e., index-guiding or bandgap-guiding, as a function of the principle of the light confinement (Buczynski, 2004). In particular, in PCFs characterized by a solid core or by a core with a refractive index higher than the micro-structured cladding's one, light is guided as in conventional silica fibers (i.e, doped silica core surrounded by the silica cladding). In fact, light propagates in the high refractive index region by the total internal reflection (TIR) principle at the interface between the core and the low refractive index cladding. In addition, air holes periodically arranged over the fiber cross-section characterize the micro-structured silica cladding, resulting in an effective cladding index. Consequently, the TIR at the core-cladding interface is known as modified TIR and it can occur with very low core-cladding refractive index (RI) contrasts, enabling the fabrication of both core and cladding by the same material.

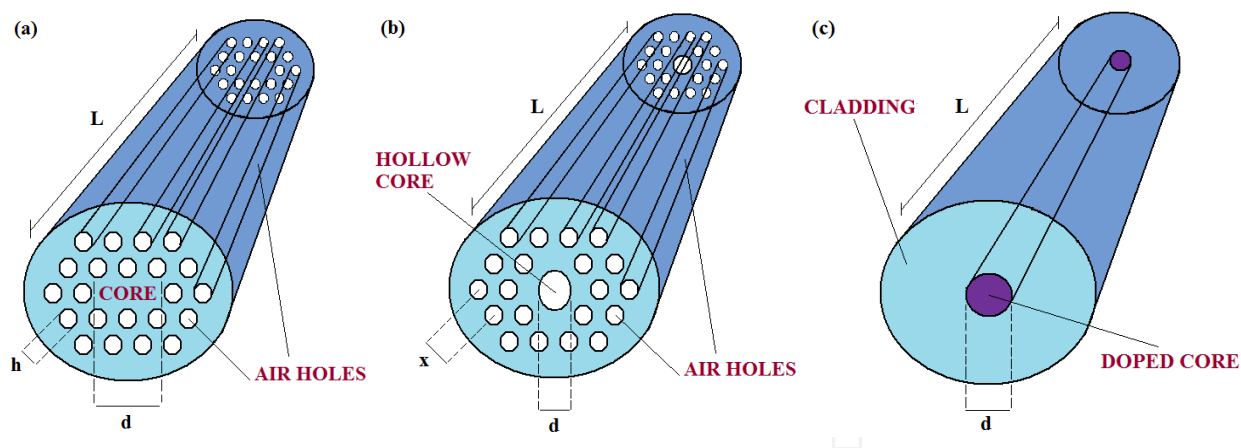


**Figure 24.** Schematic of (a) solid core PCF, (b) hollow core PCF, and (c) conventional SMF.

On the contrary, by surrounding the fiber low index core (i.e., hollow core) with a photonic crystal structure, it is possible to localize light in the fiber core by the photonic bandgap effect (Barkou et al., 1999). Consequently, only those wavelengths that do not fall within the photonic crystal stop band, can be confined in the core and propagate along the optical fiber. In this way, the TIR principle does not occur and the fiber core can be characterized by a RI lower than the cladding's one, making these optical fibers very suitable for sensing applications. In conclusion, hybrid PCF have also been theoretically and experimentally demonstrated, revealing the possibility of guiding light through simultaneous photonic bandgap-guiding and modified TIR (Xiao et al., 2007).

In both index-guiding and bandgap-guiding PCFs, the sensing mechanism consists in changing fiber optical properties (i.e., cladding effective refractive index) by filling air holes with chemical/biochemical liquids or gases. In this way, the interaction between the propagating light and the analyte to be detected is improved as it is not possible to achieve with standard optical fibers, where the sensible area is realized by removing the cladding from the fibers and directly exposing the fiber core to cover medium where the sample is concentrated.

From a technological point of view, it is possible to highlight the flexibility of the modeling and design of PCFs with respect to conventional SMFs. In fact, in a SMF the only parameter to take into account is the core diameter, while in a PCF there are three physical parameters to be properly set: the core diameter (which for solid core PCF is defined as the diameter of the ring formed by the innermost air holes), the diameter of the air holes of the cladding  $d$  and the pitch  $\Lambda$ . These three physical parameters, in combination with the choice of the refractive index of the material and the type of lattice, make the fabrication of PCFs very flexible and open up the possibility to manage its properties leading to a freedom of design not possible with common fibers.

In addition, the principal method of fabrication of PCF is the so called multiple thinning (Buczynski, 2004). In summary, the method consists of four fundamental steps: creation of individual capillaries, formation of the preform, drawing of intermediate preform, and finally,

drawing of the final fiber. In particular, in the last step extra layers of polymer are usually added to create a coating protecting the fiber mechanically.

PCFs have been widely used in sensing applications because of their ultra-high sensitivity, selectivity and immunity to optical noise and to external interferences. According to an exhaustive review on PCF sensors already published (Pinto et al., 2012), it is convenient to distinguish between physical and biochemical PCF-based sensors. In particular, physical PCF sensors are designed and implemented for measuring and monitoring physical parameters such as temperature, strain, refractive index, pressure, electromagnetic field, vibration, to be named. Moreover, PCF-based chemical and biochemical sensors are usually employed for gas sensing (e.g. acetylene, methane, oxygen), molecular and protein detection, humidity and pH monitoring.

### 3.1. Photonic crystal fiber sensors for physical sensing

In this paragraph, PCF sensors are investigated in detail, focusing on design criteria and measurement setups usually employed in sensing procedures. To this purpose, by firstly considering the class of PCF physical sensors, an highly sensitive torsion sensor has been experimentally demonstrated by incorporating a segment of novel side-leakage PCF (Chen et al., 2011). In Fig. 25, the cross-section of the fabricated PCF and the relevant experimental setup are sketched.

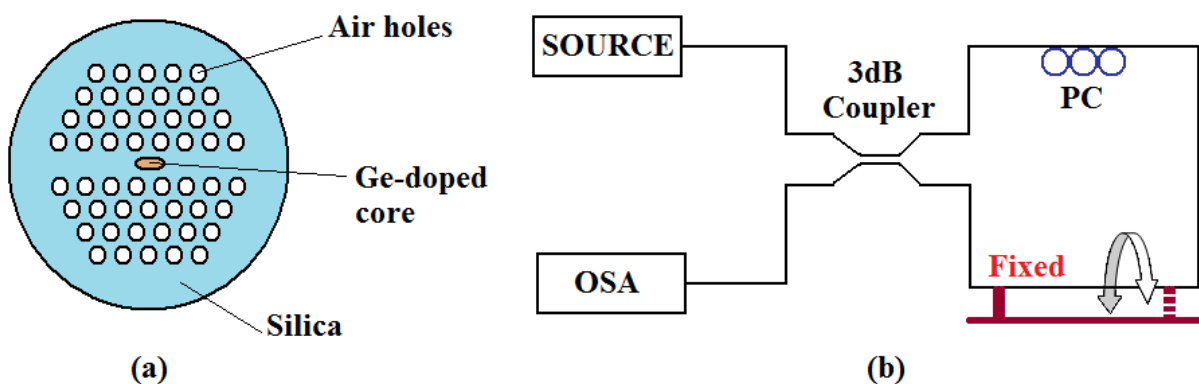


**Figure 25.** Schematics of the (a) Ge-doped PCF cross-section and (b) of the experimental setup for torsion sensing.

The fiber is characterized by a  $125\ \mu\text{m}$  cladding diameter. The elliptical Ge-doped core, adopted to introduce the fiber birefringence, is characterized by the major diameter of  $4\ \mu\text{m}$  while the minor one is equal to  $2.88\ \mu\text{m}$ . Moreover, the diameter and the pitch of air holes are  $\sim 5.48\ \mu\text{m}$  and  $\sim 8.06\ \mu\text{m}$ , respectively. The experimental setup equipped for torsion sensing is based on the Sagnac interferometer. In particular, it is composed by an optical source, a 3dB coupler that splits input light in two distinct optical signals counter-propagating in the Sagnac loop and by a polarization controller (PC), used for the interferometer optimization. In addition, a 14.85-cm-length segment of side-leakage photonic crystal fiber is incorporated in the Sagnac loop. As sketched in Fig. 31, one of the optical fiber extremity is fixed while the other one is not

bounded, thus it can be twisted in clockwise and counter-clockwise directions. Finally, an optical spectrum analyzer (OSA) is adopted for monitoring the output spectrum.

When the fiber is twisted, the linear defect can induce different mechanical stresses to the elliptical Ge-doped core. The combination effects of the torsion-induced circular birefringence and the intrinsic birefringence of the PCF fiber, generate an elliptical birefringence. Consequently, the elliptical birefringence is proportional to the torsion angle, and its rotary direction is determined by the torsion direction. In fact, when the PCF is twisted clockwise, the elliptical birefringence is right-rotary, on the contrary it is left-rotary when the fiber is twisted in the opposite direction. Finally, the torsion-induced wavelength shift  $\Delta\lambda$  characterizing the sensor transmission spectrum can be estimated by using the following expression:

$$\Delta\lambda = \lambda\eta b_t \Delta\tau \quad (15)$$

where  $\lambda$  is the operative wavelength,  $\eta$  is the circle birefringence ratio of the torsion-induced circle birefringence to the sum of the fiber birefringence,  $b_t$  is a constant that described the torsion-induced variation of the circle birefringence, and  $\Delta\tau$  is the torsion angle. Moreover, the wavelength shift  $\Delta\lambda$  is negative when the fiber is twisted clockwise, whereas it is positive when the fiber is twisted counter-clockwise.

Interesting results have been experimentally demonstrated with the PCF-based sensor described until now. In particular, a maximum torsion sensitivity of about 0.9354 nm/° has been achieved with a torsion angle measurement error due to the temperature effect of about 0.054 ~ 0.178 °/°C.

Generally, PCF sensors are designed to be strain and temperature independent. To this purpose, temperature insensitivity can be achieved by engineering the fiber composition and geometry. Otherwise, it can be contemplated the use of fiber Bragg grating (FBG) or long period grating (LPG) in the measurement setup, but making the sensor architecture complicated and costly (Gong et al., 2010).

A PCF-based modal interferometric torsion sensor has been investigated and experimentally tested according to the experimental setup sketched in Fig. 26 (Nalawade et al., 2012).

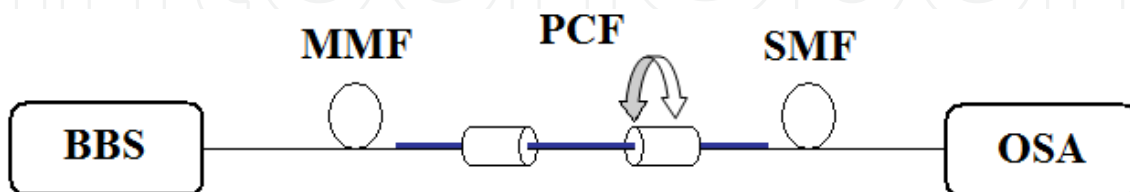


**Figure 26.** Schematic of the experimental setup (Nalawade et al., 2012).

The measurement setup consists in a broadband source (BBS), a multi-mode optical fiber for guiding the signal to the PCF and a single-mode fiber (SMF) for collecting the signal to the OSA. A torsion sensitivity of about 79.83 pm/° has been achieved in the dynamic range of 180°.

In addition, strain and temperature effects on torsion sensitivity have been demonstrated to be negligible in the range  $0\div 4500 \mu\epsilon$  and  $30\div 200 \text{ }^\circ\text{C}$ , revealing very high performance. In conclusion, sensing performance described above and other intriguing experimental results such as a torsion sensitivity of  $1 \text{ nm}/^\circ$  with a temperature sensitivity of  $-0.5 \text{ pm}/^\circ\text{C}$  in the range  $30\div 100 \text{ }^\circ\text{C}$  (Zu et al., 2011), suggest PCF-based sensors as good candidates for torsion sensing.

PCFs have been widely used in industry and reservoir engineering for monitoring fundamental parameters such as temperature and pressure. To this purpose, high performance have been theoretically demonstrated by using a PCF-based sensor, as in Fig. 27 (Padidar et al., 2012):

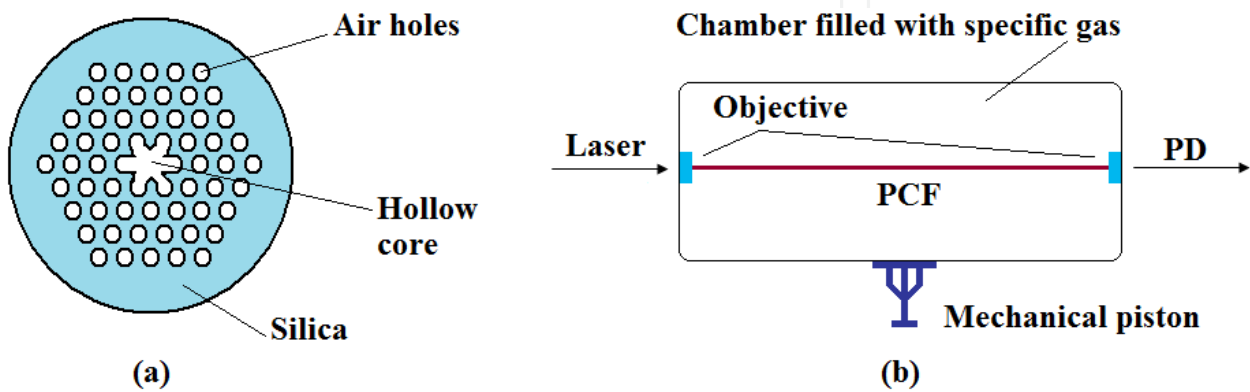


**Figure 27.** (a) Cross section of the PCF fiber and (b) schematic of the PCF-based pressure/temperature sensor.

As sketched in Fig. 27(a), the PCF cross section is characterized by air holes properly designed and periodically surrounding the inner hollow core. Consequently, this device has been designed for operating by the band-gap guiding principle, making the sensor proposed extremely selective in terms of operative wavelength. According to Fig. 27(b), the PCF described until now is fixed in a chamber filled with a specific gas. Moreover, left fiber tip receives input light at  $\lambda = 1.55 \mu\text{m}$  emitted by a laser source and the remaining tip guides the propagating light at the photo-detector (PD).

The sensor mechanism is based on the transmission peak wavelength shift induced by the temperature/pressure changes. In particular, it is needed to distinguish between the pressure and temperature sensing principle. In fact, when the sensor is used for pressure measurement, a mechanical piston (see Fig. 33b) can move due to pressure of oil well environmental. This causes the chamber gas to be compressed in high pressure or be dispersed in low pressure. Consequently, the refractive index of the specific gas filling PCF holes changes leading to a variation of photonic band gap and fundamental modes of PCF. Moreover, the wavelength sensitivity expressed in  $\text{nm}/\text{RIU}$  and previously defined in Eq. (4) can be applied also in this kind of PCF sensing application, indicating analogous sensing performance.

The mechanical piston is not yet used when the PCF-based sensor operates as temperature sensor. In particular, thermal gradients induce gas RI changes and, consequently, operative wavelength shifts, according to Eq. (4). Obviously, the filling gas has to be properly chosen such as its thermo-optic coefficient is high enough for ensuring appreciable sensitivity. This

approach is used also for making the temperature effects negligible when the sensor is used for pressure monitoring. In fact, the filling gas is chosen such as its thermo-optic coefficient has opposite sign with respect to the silica's one. In this way, silica and gas RI changes due to temperature influences can be properly compensated, resulting in the possibility of completely removing temperature effects.

In conclusion, the optimized PCF-based sensor architecture, characterized by a PCF with a length of 0.25-mm, exhibits a sensitivity of about 480 nm/RIU.

Several measurement setups based on PCFs have been widely investigated for optimizing pressure sensing performance. In particular, one of the most popular is the polarimetric measurement. This principle consists in monitoring the light intensity at the sensor output, modulated by the effect of applied pressure. In particular, by using input and output linear polarizers it is possible to control the passage of only certain orientations of plane polarized light, properly set by the input polarizer. Polarization changes induced by pressure influence, alter the current state of light polarization proportionally to the pressure strength. Consequently, if the state of polarization at the sensor output is not equal to that of the output polarizer, propagation of light is inhibited resulting in a light intensity reduction.

In this contest, an intensity measurement of pressure variation has been demonstrated, resulting in a device sensitivity of  $2.34 \times 10^{-6} \text{ MPa}^{-1}$  (Gahir et al., 2007). In addition, a high birefringence photonic crystal fiber (Hi-Bi PCF) has been designed and fabricated for realizing an hydrostatic pressure sensor based on a bidirectional modal interferometer, as sketched in Fig. 28 (Favero et al., 2010).

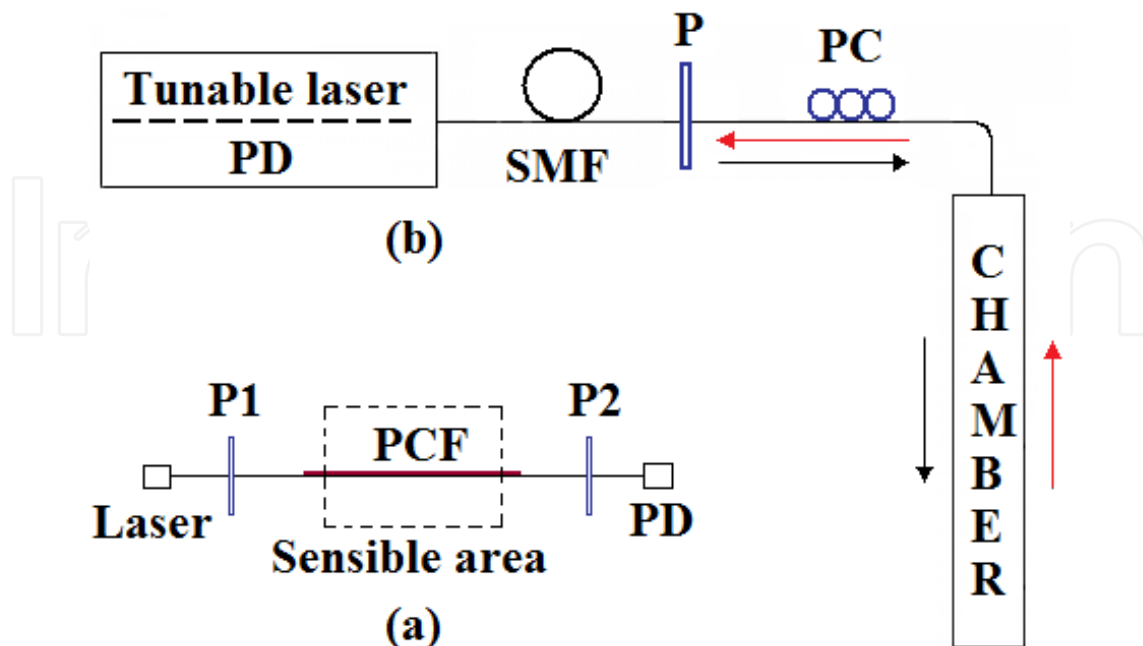


**Figure 28.** (a) Unidirectional and (b) bidirectional polarimetric measurement scheme used for pressure sensing.

In Fig. 28, it is possible to appreciate the difference between a conventional unidirectional polarimetric measurement scheme, Fig. 28(a), and a bidirectional one, Fig. 28(b). In particular, in the latter one only one polarizer (P) is used in combination with a polarization controller (PC). In the scheme proposed by Favero et al., two orthogonally polarized modes of a high birefringence PCF generate fringes over the optical spectrum of a BBS. In particular, the phase difference between the two modes, indicated with  $\varphi$ , depends on the hydrostatic pressure  $P$ , the sensor length  $L$ , and the wavelength  $\lambda$ , according to the following expression, being  $B$  the phase modal birefringence:

$$\varphi(\lambda, P, L) = \frac{4\pi L}{\lambda} B(\lambda, P) \quad (16)$$

In conclusion, the wavelength measurement of pressure has been numerically and experimentally demonstrated, revealing a sensitivity of 3.38 nm/MPa with an operating limit of 92 MPa.

Polarimetric measurement sensor schemes have been also adopted for temperature sensing. To this purpose, a Hi-Bi PCF has been used for a polarimetric interrogation revealing a sensitivity of 0.136 rad/°C at the operative wavelength of 1310 nm (Ju et al., 2006).

PCFs represent an intriguing and efficient alternative to conventional electrical (E-Field) and magnetic field (H-Field) sensors such as antennas, metal connections and conductive electrodes. The most important advantages of PCF-based E- and H-Field sensors over conventional ones are their immunity to electromagnetic interferences (apart from the sensor head), dielectric isolation between the sensor and the interrogation system and the capability to be used in harmful and remote locations.

To this purpose, an all-fiber sensor based on a nematic liquid crystal infiltrated photonic crystal fiber has been demonstrated as a directional E-Field sensor (Mathews et al., 2011a). In particular, a 1mm-long infiltrated polarization maintaining photonic crystal fiber (PMPCF) is used as sensor head. The length of the infiltrated section of the PCF, subjected to electric field, is initially optimized to have a monolithically varying polarized transmission response with electric field intensity change at 1550 nm. On selective infiltration of the two large holes characterizing the PMPCF, the birefringence of the fiber is set by the refractive indices of the nematic liquid crystal mixture, which vary as its molecules re-orientate on the application of electric field.

The transmitted intensity of the linearly polarized light with the direction of polarization at 45° with respect to the PCF polarization axis, is given by the following expression:

$$I = \frac{I_0}{2} \left\{ 1 + \sin \left( \Phi_0 + \left( \frac{\pi \Delta E}{E_\pi} \right) \right) \right\} \quad (17)$$

where  $\Phi_0$  and  $I_0$  are the inherent phase retardances due to the infiltrated PMPCF and the light intensity in the absence of field, respectively. The field induced phase retardance can be expressed as follows:

$$\Phi_E = (\pi \Delta E / E_\pi) \quad (18)$$

where  $E_\pi$  is the sensor characterization term, which is inversely proportional to the infiltration length. Finally, interesting performance have been experimentally demonstrated such as an angular sensitivity of the PMPCF orientation with respect to the electric field as -0.07 dB/degree at a fixed electric field intensity of 3.67 kV<sub>rms</sub>/mm. The sensor sensitivity to E-fields oriented parallel to the PCF polarization axis is the highest.

A polarimetric sensing scheme with selectively liquid-core infiltrated Hi-Bi PCF has been demonstrated for E-field sensing, exhibiting a sensitivity of ~ 2 dB per kV<sub>rms</sub>/mm (Mathews et al., 2011b).

In conclusion, an H-Field sensor based on Terfenol coated PCF has been fabricated and experimentally tested (Quintero et al., 2011). In this context, the Faraday effect is generally used for detecting and monitoring electric field current using optical fibers. In particular, the light polarization rotation can be expressed as a function of the magnetic flux  $B$ , the interaction length  $d$  of the propagating optical field and the magnetic field to be sensed, and of the Verdet's constant  $v$  as in the following equation:

$$\beta = vBd \quad (19)$$

It is intuitive that, for enhancing the light polarization rotation induced by the H-Field, it is possible to increase the fiber length or using fiber materials characterized by an higher Verdet's constant. The first approach is generally avoided because of the necessity of realizing optical compact sensors preventing, at the same time, high propagation losses. The second approach can be obtained by using some soft glasses for fiber optic fabrication, with the disadvantage of being mechanically fragile and temperature sensible. To this purpose, an intriguing alternative is represented by the use of Terfenol particles into optical fibers because of their high magnetostriction properties. In particular, the H-Field sensors proposed by Quintero et al., consists in a HiBi PCF made by a magnetostrictive composite using Terfenol particles with size of 250  $\mu\text{m}$  and a cycloaliphatic epoxy resin with a 30 % volume fraction of Terfenol-D.

In Fig. 29, the measurement setup employed for H-Field sensing is sketched.

The proposed PCF sensor is based on a modal interferometer, where the phase difference between the two orthogonally polarized fiber modes along the optical path generates fringes over a broadband propagation spectrum. By exposing the sensor head to a magnetic field, the magnetostrictive composite changes size, resulting in a conversion of the magnetic energy into a mechanical strain. In particular, the composite deformation causes changes of the cavity length and of the effective RI of the propagating light. Consequently, the number of fringes as

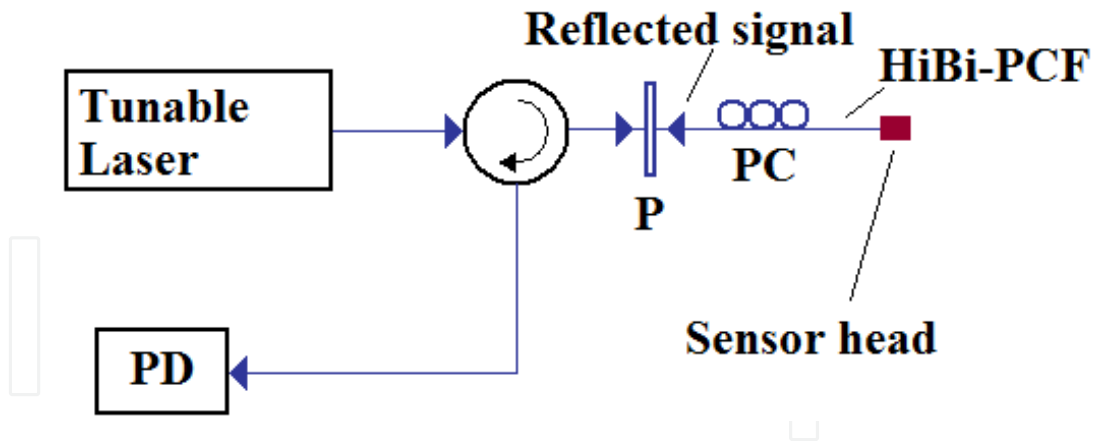


**Figure 29.** Schematic of the measurement setup of the magnetic field sensor.

well as the distance between consecutive fringes will change, both depending on the cavity length and effective index. In conclusion, experimental results evidence how the optical spectrum shifts towards longer wavelengths as the magnetic field increases, exhibiting a sensitivity of 0.006 nm/mT over a range extended from 0 to 300 mT, with a resolution of about  $\pm 1$  mT.

Nowadays, strain monitoring represents a very important sensing approach in several application areas such as aeronautics, metallurgy, health monitoring of complex structures, to name a few. Recently, a novel strain sensor has been experimentally demonstrated (Hu et al., 2012). In particular, the sensor is based on a modified PCF-based MZI characterized by three collapsed regions, as sketched in Fig. 30.

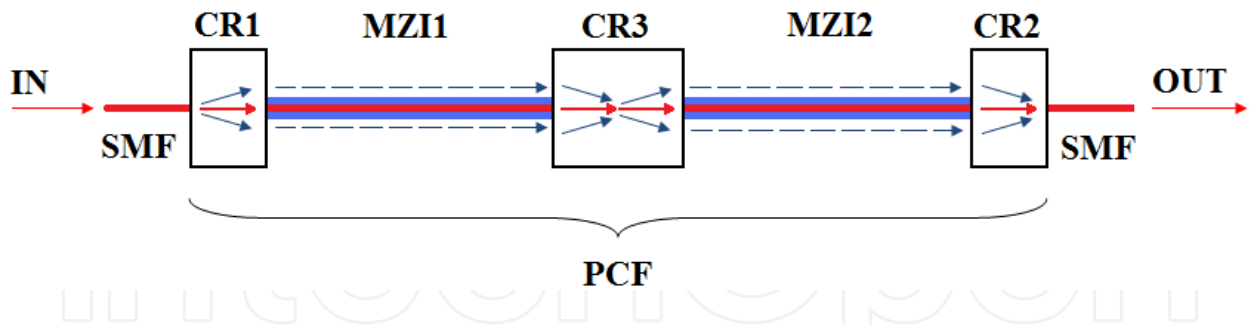


**Figure 30.** Schematic of the PCF-based MZI strain sensor.

The main advantage of using the modified PCF-based MZI configuration over the conventional MZI scheme, consists in a significantly enhanced extinction ratio of the transmission spectrum, resulting in an increased measurement accuracy. In collapsed regions (CR), realized by collapsing air holes with heat-treatment (Magi et al., 2005), the PCF is not a SMF because there is not any core-cladding structure. A part of the optical beam coming from the core of the lead-in SMF will be coupled into cladding modes in CR1. Then, the two beams propagating along the core and cladding of the PCF will combine and interfere in the collapsed regions CR3 and CR2, successively. Therefore, the modified PCF-MZI is actually a combined one with two

cascaded MZIs (indicated with MZI1 and MZI2). Consequently, the interference takes place two times resulting in a higher extinction ratio at the lead-out SMF with respect to the conventional PCF-MZI.

In particular, at the end of the second MZI (i.e., MZI2), the transmission spectrum can be expressed as follows:

$$T_{MZI2} = kT_{MZI1}^2 \quad (20)$$

where  $k$  is the factor that describes the insertion loss of the transmission light at CR3 and  $T_{MZI1}$  is the total intensity of the transmission from MZI1, equal to:

$$T_{MZI1} = E_0^2 + \sum_{i=1}^n E_i^2 + 2 \sum_{i=1}^n \left( E_0 E_i \cos \frac{2\pi(n_0 - n_i)L}{\lambda} \right) + 2 \sum_{i=1}^{n-1} \sum_{j=i+1}^n \left( E_i E_j \cos \frac{2\pi(n_i - n_j)L}{\lambda} \right) \quad (21)$$

where  $E_0$ ,  $E_i$ , and  $E_j$  are the magnitudes of electric field of the core mode and the  $i^{\text{th}}$ - and  $j^{\text{th}}$ -order cladding mode of the PCF in MZI1, respectively. Moreover,  $n_0$ ,  $n_i$ , and  $n_j$  are the effective indices of the core mode, the  $i^{\text{th}}$ - and  $j^{\text{th}}$ -order cladding mode of the PCF in MZI1, respectively. Finally,  $L$  is the physical length of the MZI1 and MZI2 (overall PCF length  $\sim 9.2$  cm, CR1 length = CR2 length =  $135 \mu\text{m}$  and CR3 length =  $291 \mu\text{m}$ ), and  $\lambda$  is the operating wavelength of the optical source.

When an axial strain is applied on the total length of the PCF, the physical length of each cavity will change, and the effective RI for each mode of the PCF will change due to the photoelastic effect, too. Consequently, the phase differences of MZI1 and MZI2 change due to the applied strain and a wavelength shift of the interference patterns can be observed.

In conclusion, the sensor described above exhibits a sensitivity as high as  $11.22 \text{ dB/m}\epsilon$  over a range of  $1.28 \text{ m}\epsilon$  and high-temperature stability (i.e.,  $0.0015 \text{ nm}/^\circ\text{C}$  and  $0.009 \text{ dBm}/^\circ\text{C}$ ).

A birefringent interferometer configured by a polarization-maintaining photonic crystal fiber (PM-PCF), has been proposed for temperature-insensitive strain measurement (Han, 2009). The strain sensor exhibits a sensitivity of  $1.3 \text{ pm}/\mu\epsilon$  in a strain range extended from 0 to  $1600 \mu\epsilon$  and a LOD for strain measurement as low as  $2.1 \mu\epsilon$ . In conclusion, the measured temperature sensitivity is  $-0.3 \text{ pm}/^\circ\text{C}$ .

### 3.2. Photonic crystal fiber for biochemical sensing

The review on PCF sensors is completed by focusing on the class of chemical and biochemical PCF-based sensors.

PCFs are very suitable for chemical and biochemical sensing because of several unique features. In particular, in a micro-structured optical fiber the hollow core and air holes characterizing the cladding section, can be properly filled with liquid solutions or gases by

using micropumps or particular syringes. In addition, by functionalizing inner walls of voids and hollow core, it is possible to selectively immobilize chemical analytes into the optical device enhancing, in this way, the light-matter interaction. The great overlapping between the propagating optical signal and the analyte to be detected, can be further enhanced by designing PCFs with long interaction lengths. Another important feature of PCFs is their flexibility that allows to employ these sensors for advanced chemical remote sensing.

In the following, different sensing principles adopted in PCF-based sensing are described, focusing on sensor architectures and technologies used for PCFs fabrication.

To this purpose, resonant chemical and biochemical sensors based on low-RI-contrast liquid-core Bragg fibers have been experimentally demonstrated revealing ultra high performance (Qu & Skorobogatiy, 2011). In Fig. 31, the cross section of the Bragg fiber designed and fabricated for chemical and biochemical sensing, is sketched. In particular, the Bragg grating has been realized surrounding the hollow core by a periodic sequence of high and low refractive index layers. In this case, a water filled core ( $n_{Water} = 1.33$ ) is surrounded by a periodic multilayer of polymethyl methacrylate (PMMA) and polystyrene (PS), whose RIs are  $n_{PMMA} = 1.487$  and  $n_{PS} = 1.581$  at the operative wavelength  $\lambda = 650$  nm, respectively.

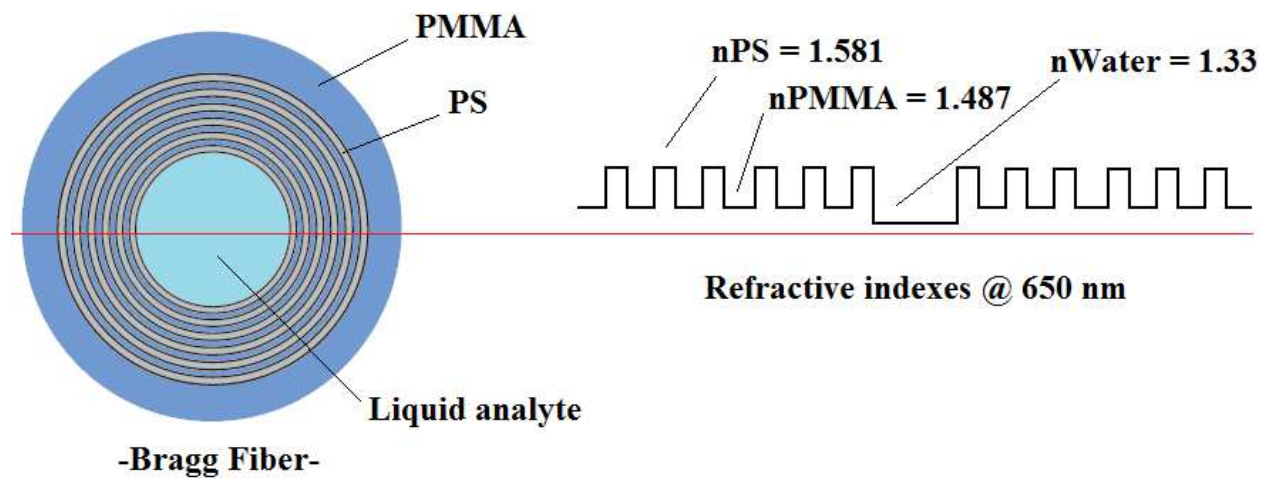


**Figure 31.** Cross section of the PMMA/PS Bragg fiber designed for chemical and biochemical sensing.

The Bragg grating is properly designed in order to exhibit a central Bragg center wavelength  $\lambda_c$  depending on optical and geometrical properties of the periodic multilayer, as reported in the equation below:

$$\frac{\lambda_c}{2} = \left[ d_h (n_h^2 - n_c^2)^{\frac{1}{2}} + d_l (n_l^2 - n_c^2)^{\frac{1}{2}} \right] \quad (22)$$

where  $d_h$  and  $d_l$  are the thickness of the low ( $n_l$ ) and high ( $n_h$ ) index layer in the Bragg reflector, and  $n_c$  is the refractive index of the liquid filled core. In the sensor proposed,  $d_h = 0.13 \mu\text{m}$ ,  $d_l =$

0.37  $\mu\text{m}$ , the number of bi-layers in the Bragg reflector is approximately 25, while refractive indices have been previously indicated in Fig. 31.

The PCF-based sensor has been experimentally tested by filling the hollow core with sodium chloride (NaCl) solutions of different concentrations. In particular, refractive indices of several NaCl solutions as a function of NaCl weight concentrations (wt.%) have been evaluated for accurate calculation (i.e., wt% = 0, 5, 10, 15, 20, 25 and corresponding RIs 1.333, 1.342, 1.351, 1.359, 1.368, 1.378).

As the NaCl concentration increases in water solution, the overall refractive index  $n_c$  proportionally increases, too. Consequently, by observing Eq. (22), it is evident that the Bragg center wavelength  $\lambda_c$  decreases, resulting in a measurable wavelength shift in the transmission spectra of the Bragg fiber. The sensor described until now exhibits an experimental sensitivity of  $\sim 1400$  nm/RIU, defined as in Eq. (4) for homogeneous sensing. In addition, the sensor has been tested also for surface sensing by detecting changes in thicknesses of thin layers deposited directly on the inner surface of the fiber core. In particular, by coating a thin layer, the localized refractive index near fiber inner surface changes, resulting in the modification of resonance guidance of the Bragg fiber, thus to the resonant wavelength shift in the Bragg fiber transmission. Moreover, if  $d_a$  is the thickness of the coated layer, the surface wavelength sensitivity can be calculated as in Eq. (23):

$$S_{\lambda,S} = \frac{\partial \lambda_c}{\partial d_a} \quad (23)$$

The presence of a 3.8- $\mu\text{m}$  thick layer of sucrose solution leads to a 3.5 nm red shift of the transmission spectrum with respect to the initial position referred to a water-filled fiber without a sucrose layer. In conclusion, a moderate sensitivity  $S_{\lambda,S} \approx 0.9$  nm/ $\mu\text{m}$  results due to poor overlap between core guided modes and the coated layer.

A PCF has been demonstrated as chemical sensor by selectively coating the fiber core with thin film containing fluorescent probe (Peng et al., 2009). The Sol-Gel method has been applied for chemical sensor functionalization. The acetylcholinesterase sensor has been experimentally tested for monitoring organophosphorus pesticide residue, revealing interesting performance. In particular, in organic pesticide parathion (PIC) and paraoxonase (Paraoxon) determination, the linear measurements ranges could arrive to  $1 \times 10^{-9} \div 1 \times 10^{-3}$  mol/L with a detection limit up to  $10^{-10}$  mol/L. In conclusion, authors suggest the PCF sensor for several application areas, such as biological/chemical research, clinical medicine, environmental protection, food inspection and preventive war biochemical fields.

A PCF interferometer operating in reflection mode has been proposed for humidity detection (Mathew et al., 2010). Generally, hygroscopic materials are required for this application field including meteorological services, air-conditioning, electronic processing, to name a few. The innovative aspect that characterized the PCF sensor proposed above, consists in the use of all-glass fiber optic based device, without using polymers or particular hygroscopic coatings.

As sketched in Fig 32, the PCF interferometer consists in a BBS, an optical spectrum analyzer (OSA), a SMF spliced to a stub of a pure silica PCF characterized by four rings of air holes arranged in a hexagonal pattern. During splicing, air holes of the PCF are completely closed resulting in a  $\sim 300\text{-}\mu\text{m}$  long collapsed region. The end section of the PCF represents the sensor head to be exposed to humidity in a climate chamber. In particular, the PCF end facet is cleaved so that the PCF behaves as a mirror. In this case, air holes are left open allowing humidity to fill in resulting in optical properties changes.

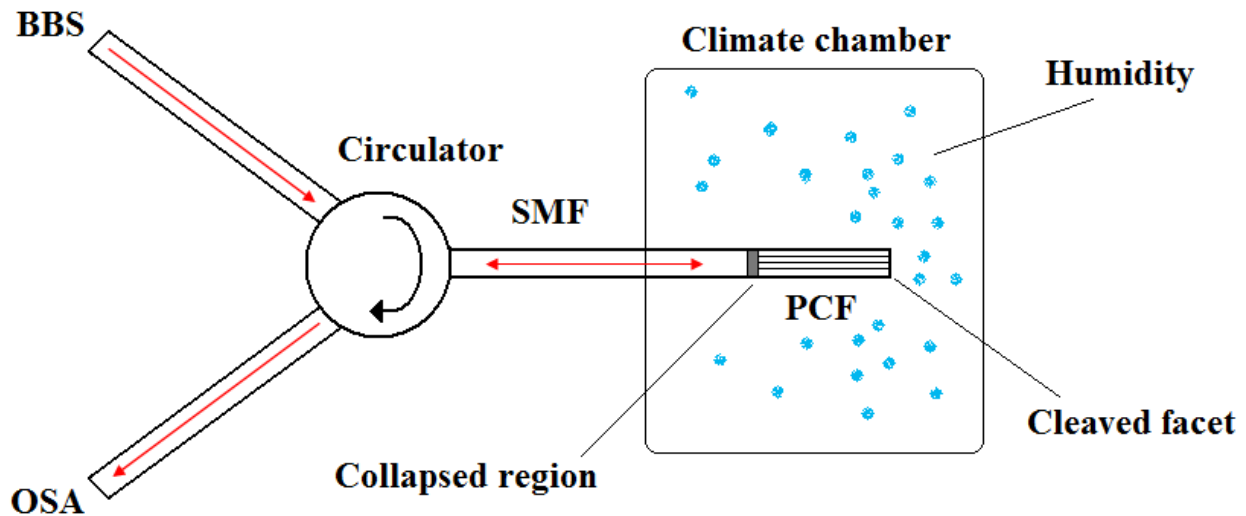


**Figure 32.** Schematic of the humidity sensor based on PCF interferometer.

The fundamental SMF mode excited by the BBS propagates to the collapse region where the excitation of two core modes occurs. These modes propagate to the cleaved PCF end facet, thus they are reflected to the collapse region where they recombine forming again a SMF fundamental mode. The recombination leads to an interference pattern whose interference peaks shift as a function of the relative humidity (RH) values in the climate chamber (i.e., the adsorption and desorption of  $\text{H}_2\text{O}$  molecules at the air-glass interface within the PCF holes). The sensitivity of the PCF interferometer sensor has been experimentally demonstrated to be about  $5.6 \text{ pm}/\% \text{RH}$  in the range extended from 40 to 70% RH. Moreover, the shift of the interference pattern is most significant above 70% RH, exhibiting a sensitivity as high as  $\sim 24 \text{ pm}/\% \text{RH}$ .

The chemical functionalization of PCF sensors represent an efficient sensing technique for the selective detection of particular analyte in chemical liquid samples properly injected in holes or hollow core, depending on the particular PCF cross section. However, this sensing approach generally requires the repetition of chemical treatments at every new measure process and the change of the functionalizing chemistry as a function of the particular analyte to be sensed by the PCF sensor. In this context, label-free PCF biosensor, in which biomolecules are unlabeled or unmodified have achieved considerable attention. Moreover, label-free sensing allows to preserve chemical properties of the specie to be detected, resulting in the possibility of executing *in vivo* analysis in addition to common *in vitro* ones.

In this context, a novel PCF-based low-index sensor has been theoretically investigated, revealing ultra high performance (Sun et al., 2011). In Fig. 33, two examples of PCF cross sections are sketched. Both PCFs are characterized by a two distinct cores. In particular, in PCF named Fiber (a) there is a pure silica core and the other core is obtained by filling air holes with liquid analyte (i.e., water with RI  $n_{Water} = 1.33$ ). In Fiber (b), the solid core is the same as that previously described, while the other core is made with an enlarged analyte-filled hole.

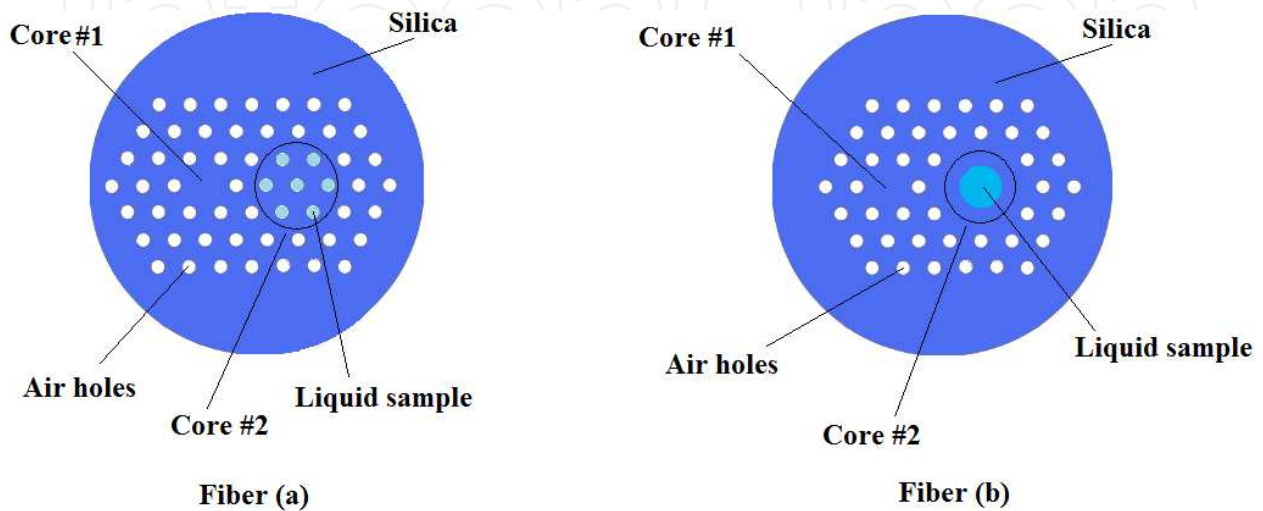


**Figure 33.** Cross sections of the analyte-filled micro-structured dual-core PCF (a), and dual-core PCF with an enlarge analyte-filled hole (b).

The resonant wavelength of the propagating optical mode can change as a function of the liquid analyte refractive index. In particular, the sensor sensitivity can be estimated according to Eq. (4). Moreover, performance results calculated by semi-vectorial beam propagation method, are listed in Table 1.

Numerical results		Fiber (a)		Fiber (b)	
Analyte refractive index	1.33	1.35	1.42	1.4	1.4
Sensitivity, S (nm/RIU)	8500	8750	12750	10750	10750
Detection limit, DL (RIU)	$2.02 \times 10^{-6}$	$1.54 \times 10^{-6}$	$2.94 \times 10^{-7}$	$4.75 \times 10^{-6}$	$4.75 \times 10^{-6}$

**Table 1.** Sensing performance of microstructured optical fiber simulated by semi-vectorial beam propagation method.

In conclusion, ultra-sensitive microstructured optical fiber refractive index sensor described until now, are able to detect liquid analyte characterized by a refractive index lower than that of the background, thus extending their regime of operation to low index liquid sample such as water.

An all-solid twin-core photonic bandgap fiber has been also designed and simulated for refractive index sensing (Yuan et al., 2010). In particular, two solid cores are separated by a

analyte-filled single hole acting as a microfluidic channel. By operating in the bandgap guiding regime the proposed sensor is capable of measuring low refractive indices around that of water (i.e.,  $n_{\text{Water}} = 1.33$ ), revealing a theoretical sensitivity as high as 70,000 nm/RIU.

A refractive index sensor based on a PCF interferometer has been recently designed and experimentally tested, revealing very interesting performance (Wang & Tang, 2012). In particular, the sensor configuration is constituted by a single MZI realized by fusion splicing a short section of PCF between two standard SMFs. The operation principle is analogous to that already described in the sensor configuration based on two cascade PCF-based MZIs (Hu et al., 2012). In particular, the excitation and recombination of cladding modes in collapsed regions lead to a transmission spectrum characterized by sinusoidal interference pattern which shifts differently when the cladding/core surface of the PCF is immersed with different RI of the surrounding medium. Interesting performance have been experimentally demonstrated by using wavelength-shift interrogation. In particular, two PCF sensor configurations, i.e. sensing length for 3.5 and 5 cm, have been exposed to different concentrations of sucrose solution revealing resolutions ranging in  $1.62 \times 10^{-4} \div 8.88 \times 10^{-4}$  RIU for the 3-cm sensor long and  $1.02 \times 10^{-4} \div 9.04 \times 10^{-4}$  RIU for the 5-cm sensor long. Sensing performance reported above have been achieved for refractive indices in the range 1.333–1.422, suggesting these sensors as suitable for biochemical sensing and environmental monitoring applications.

Recently, research efforts concerning PhC-based sensors are oriented to the optimization of light-matter interaction, with the aim to increase sensing performance. In this context, novel PCF are proposed for advanced chemical and biochemical sensing. In particular, a index-guided PCF characterized by a hollow high index ring defect at the center of its cross-section, has been proposed and theoretically investigated (Park et al., 2011). The PCF cross section is sketched in Fig. 34.

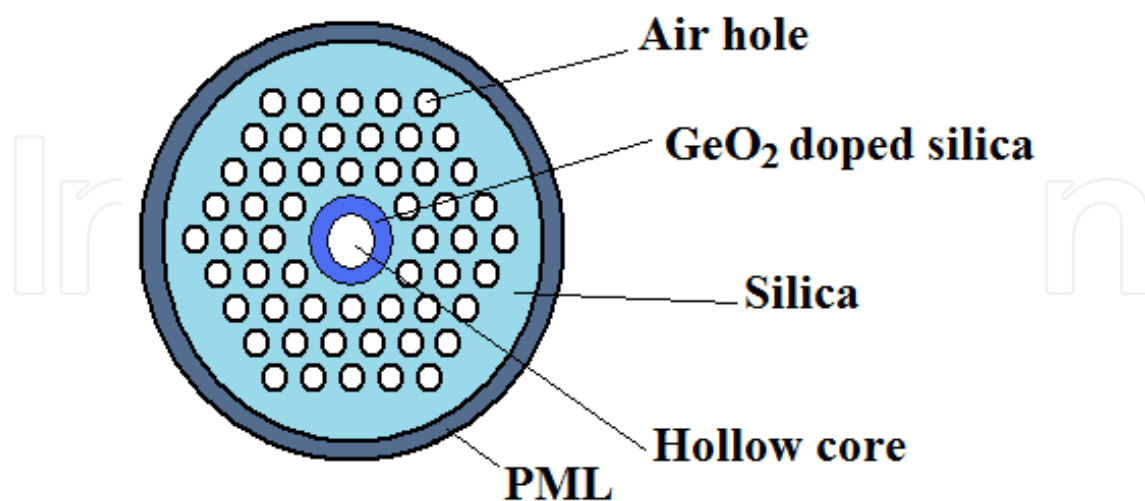


**Figure 34.** Cross section of the PCF characterized by a hollow GeO<sub>2</sub>-doped high index ring defect.

As shown in Fig. 34, the PCF cross section is characterized by a periodic distribution of air holes surrounding the high index GeO<sub>2</sub>-doped silica ring defect. A perfect matched layer (PML) is

used for numerical analysis. In particular, theoretical simulations reveal an high mode intensity distribution inside the ring defect, i.e., the high refractive index region. Finally, the proposed PCF designed with optimal parameters, exhibits a relative sensitivity as high as 5.09%, and a confinement loss as low as 1.25 dB/m, suggesting this hollow core architecture as suitable for biochemical sensing, such as for the characterization of gas species (Dicaire et al., 2010). In this context, a PCF spliced to a standard optical fiber, has been arranged in an interferometer sensing scheme for detecting volatile organic compounds (VOCs) (Villatoro et al., 2009). In particular, the PCF consists of five rings of air holes arranged in a hexagonal pattern and guides light by means of the internal reflection effect. The PCF voids have been experimentally infiltrated with vapors of methyl alcohol (CH<sub>3</sub>OH), acetonitrile (CH<sub>3</sub>CN), isopropanol (C<sub>3</sub>H<sub>6</sub>OH), or tetrahydrofuran (THF), without using any permeable material. The sensing mechanism, as previously analyzed for interferometer sensing architectures, consists in the variation of the effective cladding index induced by the presence of VOCs in air holes. In this way, the reflection spectrum characterized by a regular interference pattern, is affected by interference peak shifts proportional to refractive index changes. The proposed sensor based on PCF interferometer has been fabricated and experimentally characterized, revealing interesting performance. In particular, detection limits can be estimated by associating the maximum shifts observed in the interference pattern of the reflection spectrum with the maximum volume that can be housed in air voids, i.e., ~520 picoliter. Consequently, with THF the amount of VOC detected in this low volume lies in the ~4×10<sup>-10</sup> mole range, for acetonitrile this value is ~10.5×10<sup>-10</sup> moles. Finally, the sensor proposed is able to detect in the few hundreds or thousands of picomoles (10<sup>-12</sup>) range for VOCs, as previously presented. In this way, the sensor can be used for advanced biochemical applications, such as trace chemical or gas detection.

The review on PCF biochemical sensors includes also the so called long-period fiber grating (LPG). In particular, a LPG is a one dimension (1D) periodic structure formed by introducing periodic modulation of the refractive index along the optical fiber. LPG resonantly couples light from the fundamental core mode to some co-propagating cladding modes and leads to dips in the transmission spectrum. LPGs have been widely used for sensing purposes, such as strain, temperature and biochemical detection (Massaro, 2012). In this context, long-period gratings in photonic crystal fibers (PCF-LPG) have been experimentally demonstrated and used for label-free detection of biomolecules (Rindorf et al., 2006). In Fig. 35, a schematic of the cross section of the PCF-LPG is shown.

The sensor proposed has been functionalized with poly-L-lysine (PLL) in order to selectively immobilize charged DNA molecules on hole surfaces (see Fig. 41b). In particular, the PLL and DNA layers are characterized by refractive indices in the range 1.45÷1.48, thus closer to that of silica (1.453 @ 850 nm) than that of H<sub>2</sub>O (1.328 @ 850 nm, 25°C).

A deep in the transmission spectrum of the PCF-LPG sensor can be experimentally appreciated at the resonant wavelength  $\lambda_R$  of the LPG. Moreover, the resonant wavelength can be expressed as follows:

$$\lambda_R = \Lambda_G \left( n_{co}^{eff}(\lambda) - n_{cl}^{eff}(\lambda) \right) \quad (24)$$

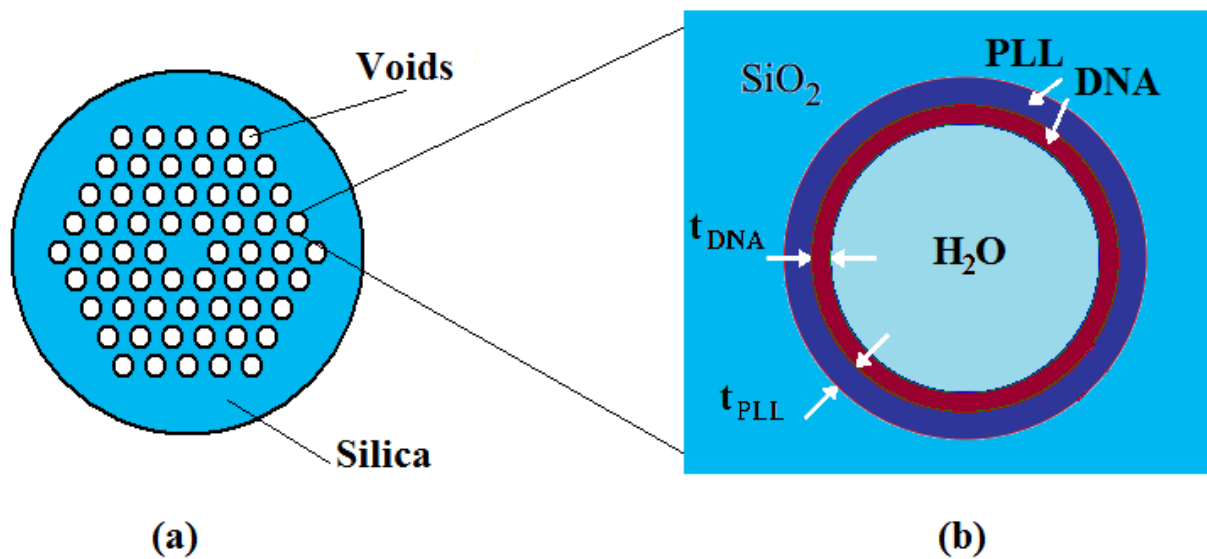


**Figure 35.** Cross section of the PCF used as sensitive biochemical sensor (a). Single void hole filled with water and functionalized with poly-L-lysine (PLL) of thickness  $t_{PLL}$  on which the DNA layer of thickness  $t_{DNA}$  is adsorbed (b).

where,  $\Lambda_C$  is the period of the LPG and  $n_{co}^{eff}(\lambda)$  and  $n_{cl}^{eff}(\lambda)$  are the effective indexes of core and cladding modes as a function of the free-space wavelength, respectively.

The resonant wavelength of the LPG when air is inside holes, is measured to be  $\lambda_{Air} = 753.6$  nm. Successively, voids have been filled with phosphate buffered saline solution (PBS) resulting in a shifted resonant wavelength  $\lambda_{PBS} = 842.5$ . Moreover, the immobilization of PLL shifts the resonant wavelength to  $\lambda_{PLL} = 849.2$  nm, and when DNA is adsorbed on the functionalized surface the new  $\lambda_R$  is measured to be  $\lambda_{DNA} = 851.4$  nm. The average thicknesses of PLL and the double-strained DNA monolayer are estimated to be  $t_{PLL} = 4.79$  nm and  $t_{DNA} = 1.65$  nm, respectively.

In conclusion, the PCF-LPG is able to detect a cladding effective refractive index change of approximately  $10^{-4}$  RIU, exhibiting a wavelength sensitivity as high as 1.4 nm/nm (i.e., the shift in resonance wavelength in nm per nm thickness of biomolecular layer).

### 3.2.1. Photonic crystal fiber sensors based on nonlinear effects for biochemical sensing

Non linear effects, such as Four Wave Mixing (FWM) and surface enhanced Raman scattering (SERS) have been widely used for sensing applications.

In this context, a microstructured optical fiber (MOF) has been proposed for label-free selective biosensing of streptavidin (Ott et al., 2008). In particular, the nonlinear biosensor is based on the change in the degenerate FWM gain spectrum induced by the selective adsorption of streptavidin antigen biomolecules on the walls of the holes, properly functionalized with  $\alpha$ -streptavidin, thus the antibody in the biochemical ligand.

In degenerate FWM, two pump signals at the same frequency  $\omega$ , generate two new signals in the MOF, i.e. Stokes and anti-Stokes signals characterized by frequencies  $\omega_s$  and  $\omega_{as}$ , respec-

tively. These new signals are generated symmetrically around the pump  $\omega$  because of the principle of the energy conservation. In particular, it results that  $\omega_s = \omega - \Omega$ , and  $\omega_{as} = \omega + \Omega$ . Moreover, the gain of the degenerate FWM can be expressed as in the following expression:

$$g(\Omega) = \sqrt{(\gamma P_0)^2 - \left(\frac{\kappa}{2}\right)^2}, \quad \kappa = 2\gamma P_0 + \Delta\beta \quad (25)$$

where  $\gamma = n_2\omega_0/(cA_{eff})$  is the nonlinear parameter,  $c$  is the speed of light in vacuum,  $\omega_0$  is the pump frequency,  $n_2$  is the nonlinear refractive index of the material used for MOF fabrication (i.e.,  $n_2 = 2.6 \times 10^{-20} \text{ m}^2/\text{W}$  for silica),  $P_0$  is the peak power of the pump and  $A_{eff}$  is the effective area of the guided mode. Finally,  $\Delta\beta$  is the linear phase-mismatch expressed as follows:

$$\Delta\beta = \beta(\omega_s) + \beta(\omega_{as}) - 2\beta(\omega) \quad (26)$$

where  $\beta(\omega)$  is the linear propagation constant at the frequency  $\omega$ .

In the proposed sensor, each hole of the silica PCF is properly functionalized by forming a layer of  $\alpha$ -streptavidin with a thickness of 40 nm on the inner hole surfaces, as it has been analogously described for PLL surface functionalization, previously sketched in Fig. 35. The functionalized sensor is designed in order to exhibit precise Stokes and anti-Stokes signals around the pump frequency  $\omega$ . When streptavidin biomolecules are adsorbed onto the functionalized surface, a bio-molecular adlayer of thickness  $t_{bio} = 5 \text{ nm}$  is formed. Consequently, the hole diameter is reduced resulting in a change of the effective area of the guided mode,  $A_{eff}$ . This effect causes a change in the degenerate FWM gain, resulting in shifts of Stokes and anti-Stokes signals around the pump signal  $\omega$ . In conclusion, by tracking the Stokes and anti-Stokes frequency shifts it is possible to detect adsorbed biomolecules with ultra high performance. In fact, the nonlinear sensor described until now exhibits a wavelength sensitivity of  $\sim 10.4 \text{ nm/nm}$ , which is a factor of 7.5 higher than that achieved by Rindorf et al., previously reported to be  $1.4 \text{ nm/nm}$ .

Nowadays, one of the most important feature often required from optical biochemical sensors is the molecular specificity in addition to high sensitivity, low cost, easy fabrication, label-free, short-time detection, reusability, compactness, flexibility, to be named.

To this purpose, Raman spectroscopy represents a powerful optical technique due to its unique molecular specificity. In fact, Raman signal carries the specific vibrational information of the molecules to be sensed. The main drawback of this technique is represented by the weak of the Raman signal, especially in case of very low concentration of molecules in a complex liquid sample. In order to enhance the Raman signal, SERS has been widely used because of the possibility of amplifying the Raman signal by orders of magnitude due to the strong enhancement of the electromagnetic field by the Surface Plasmon Resonance (SPR) of the metallic nanostructures and the surface chemical enhancement. In particular, a surface plasmon is a localized electromagnetic wave that propagates along the metal-dielectric interface and

exponentially decays into both media. Surface plasmons can be excited due to the resonant transfer of the incident photon energy and momentum to collectively oscillating electrons in a noble metal (e.g., silver, gold).

In this context, liquid-core PCFs have been experimentally investigated and theoretically analyzed for biochemical sensing of various molecules such as Rhodamine B, Rhodamine 6G (R6G), human insulin, and tryptophan, revealing excellent performance (Yang et al., 2011b). Several biomolecules have been also detected at low concentrations (i.e.,  $10^{-6}$  M  $\div$   $10^{-7}$  M) by LCPCF based on SERS, such as Prostate Specific Antigen (PSA) and alpha-synuclein, which are indicators of prostate cancer and Parkinson's disease, respectively (Shi et al., 2008).

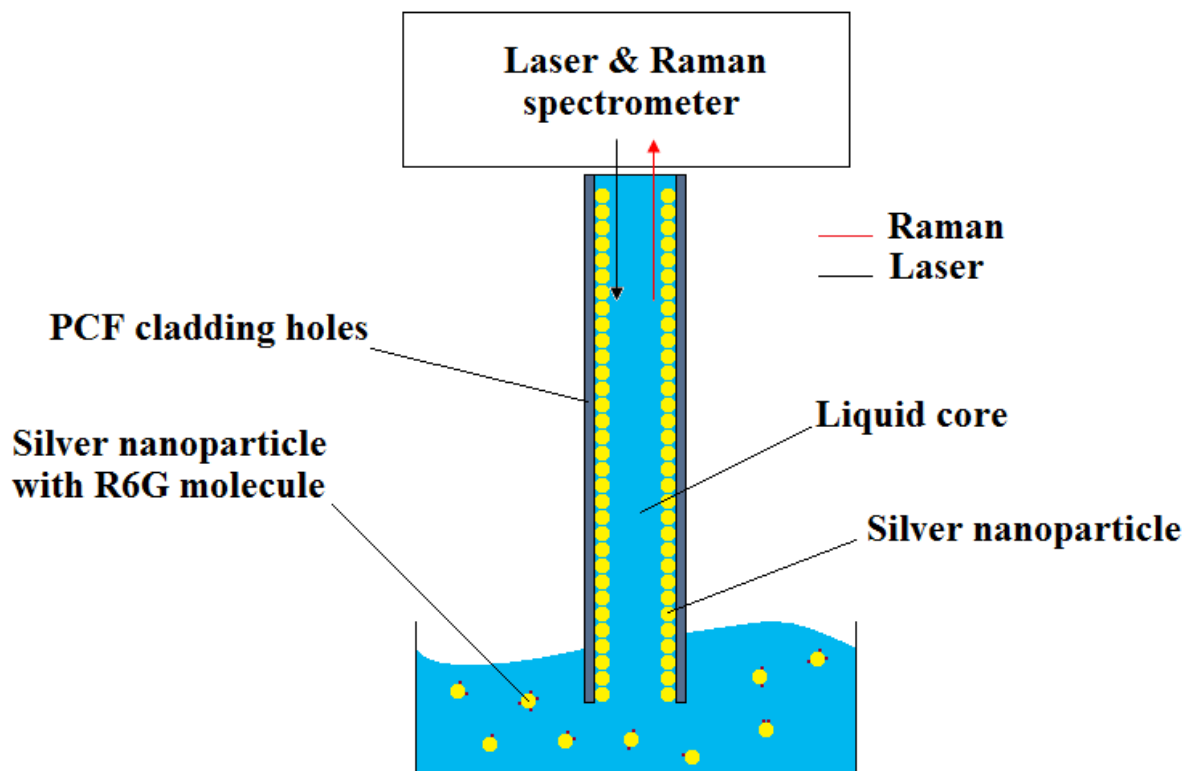


**Figure 36.** Schematic of the inner wall-coated LCPCF sensor used for R6G detection (Yang et al., 2011b).

In Fig. 36, the schematic of the functionalized inner wall-coated of LCPCF employed for R6G detection is sketched. The optical signal emitted by the laser source propagates along the LCPCF and excites the SPR at the surface of silver nanoparticles (SNPs). Some of these metal particles have attached on their surfaces R6G molecules to be detected. Consequently, the enhanced Raman signal containing detailed molecule vibrational information, counter-propagates to the Raman spectrometer in order to be analysed.

Interesting performance have been experimentally demonstrated. In fact, by using SNPs as the SERS substrate and R6G as a test molecule, the lowest detectable concentration that has been achieved is  $10^{-10}$  M.

Finally, a PCF sensor based on SERS on silver nanoparticle colloid has been experimentally demonstrated for the detection of 4-mercaptobenzoic acid (4-MBA) molecules (Xie et al., 2008). Experiments have been done by mixing 200  $\mu\text{L}$  of 0.01 mM 4-MBA aqueous solution with 100  $\mu\text{L}$  of silver colloid and by filling the mixture solution into air holes of PCF through a particular syringe setup.

### 3.2.2. Photonic crystal fiber sensors based on surface plasmon resonance

Optical sensors based on SPR have been widely used in biological sensing because of their high sensitivity, and label-free detection.

Recently, the theoretical investigation of a PCF based on SPR has been demonstrated as efficient biosensor operating in aqueous environment (Akowuah et al., 2012). The cross section of the PCF SPR sensor proposed is sketched in Fig. 37. In particular, the proposed sensor consists of two metalized microfluidic slots, air holes for light guidance and a small central air hole for facilitating phase matching between guided and Plasmon modes. Extra air holes have been inserted between the main air holes for reducing propagation losses and ensuring efficient coupling between the core guided and plasma modes.

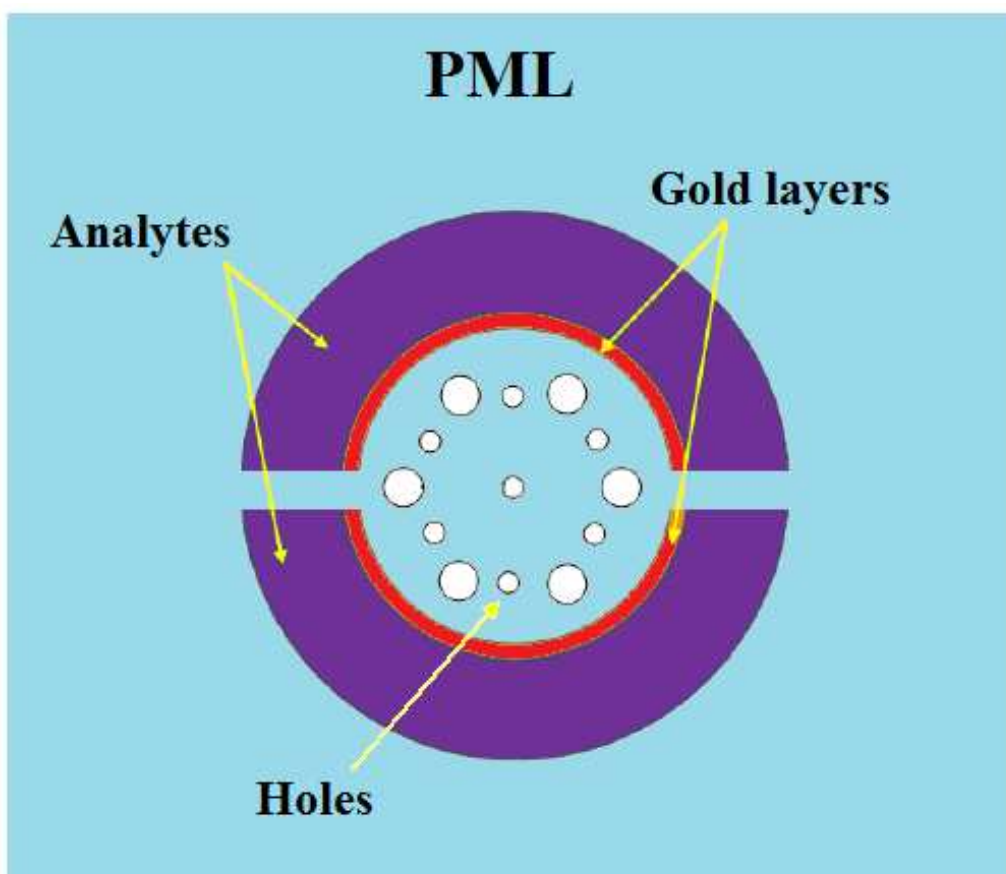


**Figure 37.** Schematic of the PCF based on SPR simulated for biochemical detection in aqueous environment.

The sensor has been simulated and optimized by using the full-vectorial Finite Element Method (FEM) with perfect matched layer (PML). In particular, when the sensor operates in the wavelength interrogation mode, changes in the analyte refractive index are detected by measuring the displacement of a plasmonic peak, and the wavelength sensitivity is defined as in Eq. (4), in which  $\lambda$  is equal to  $\lambda_p$  representing the wavelength corresponding to the SP resonance condition, in this case. Consequently, by changing the analyte refractive index from 1.33 (pure water) to 1.34, the optimized PCF SPR sensor exhibits a wavelength sensitivity as high as 4000 nm/RIU and a limit of detection as low as  $2.5 \times 10^{-5}$  RIU.

Nowadays, PCF SPR sensors are investigating for biochemical sensing because of their ultra-high performance. For example, a PCF-based refractive index sensor employing the SPR as sensing principle, has been recently theoretically investigated. In particular, sensing performance have been estimated to be  $S = 1700$  nm/RIU (refractive index sensitivity), and  $LOD = 5.9 \times 10^{-5}$  RIU, in aqueous environment (Peng et al., 2012).

In conclusion, PCF SPR sensors are also easy to fabricate. In fact, according to Fig. 37, deposition of metal layers inside of the microfluidic slots can be performed either with the high-pressure chemical vapor deposition technique or electroless plating techniques.

## 4. Conclusions

In this chapter the state-of-the-art of PhC-based sensors has been reviewed focusing on principal features and advantages of different architectures and measurement setups presented in literature.

In case of integrated PhC-based sensors, the most common physical principle is the RI sensing employed for detection of particles, gases, chemical and biological molecules, proteins, viruses, salinity in water, to name a few. In addition to other sensing principles usually employed in PhC-based sensing (i.e., optical absorption, nonlinear effect), SPR and fluorescence have been also investigated, revealing intriguing performance in detection of DNA (Mathias et al., 2010), immunoglobulin G (IgG), Goat anti-Human IgG, bovine serum albumin (BSA) in phosphate buffered saline (PBS) and Cysteamine (Huang et al., 2008).

Interferometric architectures and photonic sensors based on resonant microcavities represent undoubtedly the most efficient integrated solutions for ultra high sensing performance and simple optical and CMOS-compatible readouts. In this context, typical value of wavelength sensitivities are of the order of  $S_\lambda = 298$  nm/RIU achieved by a slot-waveguide-based ring resonator (Claes et al. 2009) and  $S_\lambda = 26$  nm/RIU exhibited by a Mach-Zehnder configuration (Lu et al., 2009). In comparison with performance mentioned above, resonant PhC cavities have been demonstrated to be able to achieve higher wavelength sensitivities as high as  $S_\lambda = 460$  nm/RIU and  $S_\lambda = 570$  nm/RIU.

The principal disadvantage characterizing PhC-based sensors is represented by the rigorous control of technological processes to be executed during design and fabrication. These

requirements are necessary because of nanometric sizes of defects and holes in PhC periodic structure and the very high sensor operating sensitivity with respect to geometrical and physical changes. Anyways, the well-known SOI technological platform identifies a cheap and standard facility for the mass-scale production of PhC-based sensors.

Photonic crystal fibers represent a very efficient sensing solution for industrial, medical and environmental applications.

In fact, due to their fabrication simplicity, high fabrication tolerances and other advantages such as immunity to external effects, PCFs are usually employed for remote sensing in dangerous and harmful environments. Strategic approaches for improving sensing performance concern with PCF technological optimization, selection of suitable materials to be employed for sensing purposes (e.g., sol-gel, polymers), and the development of efficient and innovate measurement setups for improving readout capabilities.

Finally, photonic crystal technology surely represents a research field to be further investigated for its incredible potential in applications such as optical signal processing, telecommunications and, last but not the least, advanced optical sensing.

## Author details

Benedetto Troia, Antonia Paolicelli, Francesco De Leonardis and Vittorio M. N. Passaro

Photonics Research Group, Dipartimento di Elettrotecnica ed Elettronica, Politecnico di Bari, Italy

## References

- [1] Akowuah, E.K.; Gorman, T; Ademgil, H.; Haxha, S.; Robinson, G. & Oliver, J. (2012). A Novel Compact Photonic Crystal Fibre Surface Plasmon Resonance Biosensor for an Aqueous Environment. *Photonic Crystals - Innovative Systems, Lasers and Waveguides*, A. Massaro (Ed.), 978-953-51-0416-2, InTech.
- [2] Arunbabu, D.; Sannigrahi, A. & Jana, T. (2011). Photonic crystal hydrogel material for the sensing of toxic mercury ions ( $Hg^{2+}$ ) in water. *Soft Matter*, (February 2011), 7(6), 2592-2599.
- [3] Awad, H.; Hasan, I.; Mnaymneh, K.; Hall, T.J. & Andonovic, I. (2011). Gas sensing using slow light in photonic crystal waveguide. *7th Workshop on Fibre and Optical Passive Components (WFOPC)*, 978-1-4577-0861-9, (July 2011), 1-3.
- [4] Bakhtazad, A.; Sabarinathan, J. & Hutter, J.L. (2010). Mechanical Sensitivity Enhancement of Silicon Based Photonic Crystal Micro-Pressure Sensor. *International Symposium on Optomechatronic Technologies (ISOT)*, 978-1-4244-7682-4, (October 2010), 1-5.

- [5] Barkou, E. S.; Broeng, J. & Bjarklev, A. (1999). Dispersion properties of photonic bandgap guiding fibers. OFC/IOOC ©99. Technical Digest, (February 1999), 4, 117-119.
- [6] Biallo, D.; D'Orazio, A.; De Sario, M.; Marrocco, V. & Petruzzelli, V. (2006). Proceedings of 2006 International Conference on Transparent Optical Networks (ICTON), (June 2006), 2, 44-48.
- [7] Bougriou, F.; Bouchemat, T.; Bouchemat, M. & Paraire N. (2011). High sensitivity of sensors based on two-dimensional photonic crystal. Electronics, Communications and Photonics Conference (SIEPCPC), 2011 Saudi International. 978-1-4577-0069-9, (April 2011), 1-4.
- [8] Buczynski, R. (2004). Photonic Crystal Fibers, *Acta Physica Polonica A*, 106(2), 141-167.
- [9] Chakravarty, S.; Lai, W.-C.; Zou, Y.; Lin, C.; Wang, X. & Chen, R.T. (2011a). Silicon-nanomembrane-based photonic crystal nanostructures for chip-integrated open sensor systems. *Proceeding of SPIE*, (November 2011), art. 819802, 8198.
- [10] Chakravarty, S.; Lai, W.-C.; Wang, X.; Lin, C. & Chen, R.T. (2011b). Photonic crystal slot waveguide spectrometer for detection of methane. *Proceedings of SPIE*, (January 2011), art. 79410K, 7941.
- [11] Chen, W.; Lou, S.; Wang, Liwen; Zou, H.; Lu, Wenliang & Jian, S. (2011). Highly Sensitive Torsion Sensor Based on Sagnac Interferometer Using Side-Leakage Photonic Crystal Fiber. *IEEE Photonics Technology Letters*, (November 2011), 23(21) 1639-1641.
- [12] Chen, X. & Chen, R.T. (2008). Sensitivity-enhanced silicon slot photonic crystal waveguides. 5th IEEE International Conference on Group IV Photonics, 978-1-4244-1768-1, (September 2008), 395-397.
- [13] Choi, C.J. & Cunningham, B.T. (2006). Single-step fabrication and characterization of photonic crystal biosensors with polymer microfluidic channels. *Lab on a Chip*, (August 2006), 6(10), 1373-1380.
- [14] Claes, T.; Molera, J.G.; Schacht, E.; Baets, R. & Bienstman, P. (2009). Label-Free Biosensing With Slot-Waveguide-Based Ring Resonator in Silicon on Insulator. *IEEE Photonics Journal*, (September 2009), 1(3), 197-204.
- [15] Dicaire, I.; Beugnot, J.-C. & Thevenaz, L. (2010). Optimized conditions for gas light interaction in photonic crystal fibres. *Proceedings of SPIE*, (September 2010), art. 76530L, 7653.
- [16] Endo, T.; Yanagida, Y. & Hatsuzawa, T. (2007). Photonic crystal based optical chemical sensor for environmental monitoring. 7th IEEE International Conference on Nanotechnology (IEEE-NANO 2007), 1-4244-0608-0, 947-950.
- [17] Favero, F.C.; Quintero, S.M.M; Martelli, C; Braga, A.M.B.; Silva, V.V.; Carvalho I.C.S.; Llerena, R.W.A. & Valente, L.C.G. (2010). Hydrostatic Pressure Sensing with High Birefringence Photonic Crystal Fibers. *Sensors*, (November 2010), 10(11), 9699-9711.

- [18] Gahir, H.K. & Khanna, D. (2007). Design and development of a temperature-compensated fiber optic polarimetric pressure sensor based on photonic crystal fiber at 1550 nm. *Applied Optics*, (March 2007), 46(8), 1184-1189.
- [19] García-Rupérez, J.; Toccafondo, V.; Bañuls, M.J.; Griol, A.; Castelló, J.G.; Peransi-Llopis, S. & Maquieira, A. (2010). Single strand DNA hybridization sensing using photonic crystal waveguide based sensor. 7th IEEE International Conference on Group IV Photonics, 978-1-4244-6346-6, (September 2010), 180-182.
- [20] Gong, H.P.; Chan, C. C.; Zu, P.; Chen, L. H. & Dong, X. Y. (2010). Curvature measurement by using low-birefringence photonic crystal fiber based Sagnac loop. *Optics Communication*, 283(16), 3142–3144.
- [21] Griffete, N.; Frederich, H.; Maître, A.; Chehimi, M.M.; Ravaine, S. & Mangeney, C. (2011), Photonic crystal pH sensor containing a planar defect for fast and enhanced response. *Journal of Materials Chemistry*, (July 2011), 21(34), 13052-13055.
- [22] Han, Y.G. (2009). Temperature-insensitive strain measurement using a birefringent interferometer based on a polarization-maintaining photonic crystal fiber. *Applied Physics B*, 95(2), 383-387.
- [23] Huang, H; Zhang, J.; Ji, X.; Zhou, J.; Bao, Minhang & Huang, Y. (2008). Photonic Crystal Biosensors Based on Surface Plasmons. 9th International Conference on Solid-State and Integrated-Circuit Technology (ICSICT), 978-1-4244-2186-2, (October 2008), 2565-2568.
- [24] Hu, L.M.; Chan, C.C.; Dong, X.Y.; Wang, Y.P.; Zu, P.; Wong, W.C.; Qian, W.W.& Li, T. (2012). Photonic Crystal Fiber Strain Sensor Based on Modified Mach-Zehnder Interferometer. *IEEE Photonics Journal*, (February 2012), 4(1), 114-118.
- [25] Jágerská, J.; Zhang, H.; Diao, Z.; Le Thomas, N. & Houdré, R. (2010). Refractive index sensing with an air-slot photonic crystal nanocavity. *Optics Letters*, (August 2010), 35(15), 2523-2525.
- [26] Jiang, H.; Zhu, Y.; Chen, C.; Shen, J.; Bao, H.; Peng, L.; Yang, X. & Li, C. (2012). Photonic crystal pH and metal cation sensors based on poly(vinyl alcohol) hydrogel. *New Journal of Chemistry*, (February 2012), 36(4), 1051-1056.
- [27] Ju, J.; Wang, W.; Jin, W. & Demokan, M.S. (2006). Temperature sensitivity of a two-mode photonic crystal fiber interferometric sensor. *IEEE Photonic Technology Letters*, (October 2006), 18(20), 2168-2170.
- [28] Junhua, L.; Qiang, K.; Chunxia, W.; Baoqing, S.; Yiyang, X. & Hongda, C. (2011). Design of a photonic crystal microcavity for biosensing. *Journal of Semiconductors*, (March 2011), art. 034008, 32(3).
- [29] Lee, M.; Miller, B.L. & Fauchet, P.M. (2008). Two-dimensional photonic crystal microcavity sensor for single particle detection. *Lasers and Electro-Optics, 2008 and 2008 Conference on Quantum Electronics and Laser Science*, 978-1-55752-859-9, (May 2008), 1-2.

- [30] Li, B.; Hsiao, F.L. & Lee, C. (2011). Computational Characterization of a Photonic Crystal Cantilever Sensor Using a Hexagonal Dual-Nanoring-Based Channel Drop Filter. *IEEE Transaction of Nanotechnology*, (July 2011), 10(4), 789-796.
- [31] Lin, H.; Yi, Z. & Hu, J. (2012). Double resonance 1-D photonic crystal cavities for single-molecule mid-infrared photothermal spectroscopy: theory and design. *Optics Letters*, (April 2012), 37(8), 1304-1306.
- [32] Liu, Y. & Saleemink, H.W.M. (2012). Photonic crystal-based all-optical on-chip sensor. *Optics Express*, (August 2012), 20(18), 19912-19920.
- [33] Lu, P.; Men, L.; Sooley, K. & Chen, Q. (2009). Tapered fiber Mach-Zehnder Interferometer for simultaneous measurement of refractive index and temperature. *Applied Physics Letters*, (April 2009), art. 131110, 94(13).
- [34] Magi, E.C.; Nguyen, H.C. & Eggleton, B.J. (2005). Air-hole collapse and mode transitions in microstructured fiber photonics wires. *Optics Express*, (January 2005), 13(2), 453-459.
- [35] Mandal, S. & Erickson, D. (2008). Nanoscale optofluidic sensor arrays. *Optical Express*, (February 2008), 16(3), 1623-1631.
- [36] Mandal, S.; Goddard, J.M. & Erickson, D. (2009). A multiplexed optofluidic biomolecular sensor for low mass detection. *Lab on a Chip*, (July 2009), 9(20), 2924-2932.
- [37] Massaro, A. (2012). Photonic Crystals – Introduction, Applications and Theory. A. Massaro(Ed.), 978-953-51-0431-5, InTech.
- [38] Mathew, J.; Semenova, Y.; Rajan, G. & Farrell, G. (2010). Humidity Sensor Based on a Photonic Crystal Fiber Interferometer. *Electronics Letters*, (September 2010), 46(19), 1341-1343.
- [39] Mathews, S.; Farrell, G. & Semenova, Y. (2011a). Directional electric field sensitivity of a liquid crystal infiltrated photonic crystal fiber. *IEEE Photonics Technology Letters*, (April 2011), 23(7), 408-410.
- [40] Mathews, S; Farrell, G. & Semenova, Y. (2011b). All-fiber polarimetric electric field sensing using liquid crystal infiltrated photonic crystal fibers. *Sensors and Actuators A: Physical*, (May 2011), 167(1), 54-59.
- [41] Mathias, P.C.; Jones, S.I.; Wu, H.-Y., Yang, F; Ganesh, N.; Gonzalez, D.O.; Bollero, G.; Vodkin, L.O. & Cunningham, B.T. (2010). Improved Sensitivity of DNA Microarrays Using Photonic Crystal Enhanced Fluorescence. *Analytical Chemistry*, (August 2010), 82(16), 6854-6861.
- [42] Maulina, W.; Rahmat, M.; Rustami, E.; Azis, M.; Budiarti, D.R.; Miftah, D.Y.N.; Maniur, A.; Tumanggor, A.; Sukmawati, N.; Alatas, H.; Seminar, K.B. & Yuwono, A.S. (2011), Fabrication and Characterization of NO<sub>2</sub> Gas Sensor Based on One Dimensional Photonic Crystal for Measurement of Air Pollution Index. 2nd International Conference

- on Instrumentation, Communication, Information Technology and Biomedical Engineering (ICICI-BME). 978-1-4577-1166-4, (November 2011), (2), 352-355.
- [43] Nalawade, S.M.; Harnol, S.S. & Thakur, H.V. (2012). Temperature and Strain Independent Modal Interferometric Torsion Sensor Using Photonic Crystal Fiber. *IEEE Sensors Journal*, (August 2012), 12(8), 2614-2615.
- [44] Ott, J.R.; Heuck, M.; Agger C., Rasmussen, P.D. & Bang, O. (2008). Label-free and selective nonlinear fiber-optical biosensing. *Optics Express*, (December 2008), 16(25), 20834-20847.
- [45] Padidar, S.; Ahmadi, V. & Ebnali-Heidari, M. (2012). Design of High Sensitive Pressure and Temperature Sensor Using Photonic Crystal Fiber for Downhole Application. *IEEE Photonics Journal*, (October 2012), 4(5), 1590-1599.
- [46] Park, J.; Lee, S.; Kim, S. & Oh, K. (2011). Enhancement of chemical sensing capability in a photonic crystal fiber with a hollow high index ring defect at the center. *Optics Express*, (January 2011), 19(3), 1921-1929.
- [47] Peng, Y. & Cheng, Y. (2009). The Research of photonic-crystal fiber sensor. *Proceedings of SPIE*, art. 73810G, 7381.
- [48] Peng, Y.; Hou, J.; Huang, Z.; Zhang, B. & Lu, Q. (2012). Design of the photonic crystal fiber-based surface plasmon resonance sensors. *Chinese Optics Letters*, (June 2012), art. S10607, 10(s1).
- [49] Pinto, A.M.R. & Lopez-Amo, M. (2012). Photonic Crystal Fibers for Sensing Applications. *Journal of Sensors*, art. ID 598178, (February 2012), 2012, 1-21.
- [50] Qu, H. & Skorobogatiy, M. (2012). Resonant bio- and chemical sensors using low-refractive-index-contrast liquid-core Bragg fibers. *Sensors and Actuators B: Chemical*, (January 2012), 161(1), 261-268.
- [51] Quintero, S.M.M.; Martelli, C.; Braga, A.M.B.; Valente, L.C.G. & Kato, C.C. (2011). Magnetic Field Measurements Based on Terfenol Coated Photonic Crystal Fibers. *Sensors*, (November 2011), 11(12), 11103-11111.
- [52] Rindorf, L.; Jensen, B.J.; Dufva, M.; Pedersen, H.L.; Hoiby, P.E. & Bang, O. (2006). Photonic crystal fiber long-period gratings for biochemical sensing. *Optics Express*, (September 2006), 14(18), 8224-8231.
- [53] Robinson, S. & Nakkeeran, R. (2012). Photonic Crystal based sensor for sensing the salinity of seawater. *IEEE – International Conference On Advances In Engineering, Science and Management (ICAESM)*, 978-81-909042-2-3, (March 2012), 495-499.
- [54] Scullion, M.G.; Di Falco, A. & Krauss, T.F. (2011). Slotted photonic crystal cavities with integrated microfluidics for biosensing applications. *Biosensors and Bioelectronics*, (June 2011), 27(1), 101-105.

- [55] Shi, C; Zhang, Y.; Gu, C.; Seballos, L. & Zhang, J.Z. (2008). Low Concentration Biomolecular Detection Using Liquid Core Photonic Crystal Fiber (LCPCF) SERS Sensor. *Proceedings of SPIE*, art. 685204, 6852.
- [56] Sun, B; Chen, M.-Y.; Zhang Y.-K.; Yang J.-C.; Yao, J.-Q & Cui, H.-X. (2011). Microstructured-core photonic-crystal fiber for ultra-sensing refractive index sensing. *Optics Express*, (February 2011), 19(5), 4091-4100.
- [57] Thévenaz, L.; Dicaire, I.; Chin, S. & De Rossi, A. (2012). Gas Sensing using Material and Structural Slow Light System. *Optical Sensors*, OSA Technical Digest (online) (Optical Society of America, 2012), (June 2012), paper STu2F.1
- [58] Van Driel, H.M. (2003). Nonlinear Optics in Photonic Crystal. *Proceedings of 2003 5th International Conference on Transparent Optical Networks (ICTON)*, 0-7803-7816-4, (July 2003), 1, 56-59.
- [59] Van Leest, T.; Heldens, J.; Dan Der Gaag, B. & Caro, J. (2012). Photonic crystal cavities for resonant evanescent field trapping of single bacteria. *Proceedings of the SPIE*, (June 2012), art. 84270T, 8427.
- [60] Villatoro, J.; Kreuzer, M.P.; Jha, R.; Minkovich, V. P.; Finazzi, V.; Badenes, G. & Pruneri, V. (2009). Photonic crystal fiber interferometer for chemical vapor detection with high selectivity. *Optics Express*, (February 2009), 17(3), 1447-1453.
- [61] Wang, J.-N. & Tang, J.-L. (2012). Photonic Crystal Fiber Mach-Zehnder Interferometer for Refractive Index Sensing. *Sensors*, (March 2012), 12(3), 2983-2995.
- [62] Wu, M.; Hryciw, A.C.; Khanaliloo, B.; Freeman, M.R.; Davis, J.P. & Barclay, P.E. (2012). Photonic crystal paddle nanocavities for optomechanical torsion sensing. *CLEO: Science and Innovations*, OSA Technical Digest (online) (Optical Society of America, 2012), paper CW1M.7.
- [63] Xiao, L.; Jin, W. & Demokan, M.S. (2007). Photonic crystal fibers confining light by both index-guiding and bandgap-guiding: hybrid PCFs. *Optics Express*, (November 2007), 15(24), 15637-15647.
- [64] Xie, Z.-G.; Lu, Y.-H., Wang, P.; Lin, K.-Q.; Yan, J. & Ming, H. (2008). Photonic Crystal Fibre SERS Sensors Based on Silver Nanoparticle Colloid. *Chinese Physics Letters*, (September 2008), 25(12), 4473-4475.
- [65] Yang, D.; Tian, H. & Ji, Y. (2011a). Nanoscale photonic crystal sensor arrays on monolithic substrates using side-coupled resonant cavity arrays. *Optics Express*, (October 2011), 19(21), 20023-20034.
- [66] Yang, X.; Shi C.; Newhouse, R.; Zhang, J.Z. & Gu, C. (2011b). Hollow-Core Photonic Crystal Fibers for Surface-Enhanced Raman Scattering Probes. *International Journal of Optics*, art. ID 754610, (February 2011), 2011, 1-11.
- [67] Yuan, W.; Town, E. G. & Bang, O. (2010). Refractive index Sensing in an All-solid Twin-Core Photonic Bandgap Filter. *IEEE Sensors Journal*, (July 2010), 10(7), 1192-1199.

- [68] Zlatanovic, S.; Mirkarimi, L.W.; Sigalas, M.M.; Bynum, M.A.; Chow, E.; Robotti, K. M.; Burr, G.W.; Esener, S. & Grot, A. (2009). Photonic crystal microcavity sensor for ultracompact monitoring of reaction kinetics and protein detection, *Sensors and Actuators B: Chemical*, (August 2009), 141(1), 13-19.
- [69] Zou, Y.; Chakravarty, S.; Lai, W.-C.; Lin, C.-Y. & Chen, R.T. (2012). Methods to array photonic crystal microcavities for high throughput high sensitivity biosensing on a silicon-chip based platform, *Lab Chip*, (July 2012), 12(13), 2309-2312.
- [70] Zu, P.; Chan, C.C.; Jin, Y.; Gong, T.; Zhang, Y.; Chen, L. H. & Dong, X. (2011). A temperature-insensitive twist sensor by using low-birefringence photonic-crystal-fiber-based Sagnac interferometer. *IEEE Photonics Technology Letters*, (July 2011), 23(13), 920-922.

